DFT STUDY OF ELECTRONIC STRUCTURE AND MECHANICAL PROPERTIES OF CLAY MINERALS, AND USING LARGE-SCALE SUPERCELL MODELING FOR SOLVATED MONTMORILLONITE

A DISSERTATION IN

Physics
and
Mathematics

Presented to the Faculty of the University
of Missouri–Kansas City in partial fulfillment of
the requirements for the degree

DOCTOR OF PHILOSOPHY

by

Layla Shafei

B.S. King Abdul-Aziz University, 2012
M.S. University of Missouri - Kansas City, 2016

Kansas City, Missouri
2024

DFT STUDY OF ELECTRONIC STRUCTURE AND MECHANICAL PROPERTIES OF CLAY MINERALS, AND USING LARGE-SCALE SUPERCELL MODELING FOR SOLVATED MONTMORILLONITE

Layla Shafei, Candidate for the Doctor of Philosophy Degree

University of Missouri–Kansas City, 2024

ABSTRACT

Clay mineral materials have attracted attention due to their many properties and applications. The applications of clay minerals are closely linked to their structure and composition. Here, we studied the electronic structure properties of kaolinite, muscovite, and montmorillonite crystals, which are classified as clay minerals, by using DFT-based ab initio packages VASP and the OLCAO. This work aims to have a deep understanding of clay mineral materials, including electronic structure, bond strength, mechanical properties, and optical properties. It is worth mentioning that understanding these properties may help continually result in new and innovative clay products in several applications, such as in pharmaceutical applications using kaolinite for their potential in cancer treatment, muscovite used as insulators in electrical appliances, and engineering applications that use montmorillonite as a

sealant. In addition, our results show that the role played by hydrogen bonds in O-H bonds has an impact on the hydration in these crystals. Based on calculated total bond order density, it is concluded that kaolinite is slightly more cohesive than montmorillonite, which is consistent with the calculated mechanical properties.

Montmorillonite clay (MMT) has been widely used in engineering and environmental applications as a landfill barrier and toxic waste repository due to its unique property as an expandable clay mineral that can absorb water easily. This absorption process rendered MMT to be highly exothermic due to electrostatic interactions among molecules and hydrogen bonds between surface atoms. A detailed study of a large supercell model of structural clay enables us to predict long-term nuclear waste storage. Herein, a large solvent MMT model with 4071 atoms is studied using ab initio density functional theory. The DFT calculation and analysis clarify important issues, such as bond strength, solvation effect, elasticity, and seismic wave velocities. These results are compared to our previous study on crystalline MMT (dry). The solvated MMT has reduced shear modulus (G), bulk modulus (K), and Young's modulus (E). We observe that the conduction band (CB) in the density of states (DOS) of solvated MMT model has a single, conspicuous peak at -8.5 eV. Moreover, the atom-resolved partial density of states (PDOS) summarizes the roles played by each atom in the DOS. These

findings illuminate numerous potential sophisticated applications of MMT clay.

APPROVAL PAGE

The faculty listed below, appointed by the Dean of the School of Science and Engineering, have examined a dissertation titled "DFT Study of Electronic Structure and Mechanical Properties of Clay Minerals, and Using Large-Scale Supercell Modeling for Solvated Montmorillonite" presented by Layla Shafei, candidate for the Doctor of Philosophy degree, and certify that in their opinion it is worthy of acceptance.

Supervisory Committee

Wai-Yim Ching, Ph.D. Committee Chair
Department of Physics and Astronomy

Paul Rulis, Ph.D
Department of Physics and Astronomy

Elizabeth Stoddard, Ph.D
Department of Physics and Astronomy

Noah Rhee, Ph.D.,Co-discipline Advisor
Department of Mathematics and Statistics

Majid Bani-Yaghoub, Ph.D
Department of Mathematics and Statistics

Contents

ILLUSTRATIONS

TABLES

ACKNOWLEDGMENTS

I have come to realize that achieving success is closely tied to having a virtuous support system. I am genuinely thankful to all those who have played a role in my academic success.

I want to start by expressing my gratitude to Dr. Wai-Yim Ching, my committee chair, for his exceptional mentorship, unwavering support, and insightful feedback. His expertise and dedication have been crucial in shaping my research and guiding me through the challenges of graduate school. I extend my thanks to all my committee members, Dr. Paul Rulis, Dr. Elizabeth Stoddard, Dr. Noah Rheefor, and Dr. Majid Bani-Yaghoub, for their time, energy, and dedication to my success. Their support has been pivotal in completing this dissertation.

Additionally, I want to convey deep appreciation to my family, the cornerstone of my academic journey. Despite my father's passing during my pursuit of a PhD, his dream for my success continues to light my path. I am profoundly thankful for the inspiration and encouragement that fueled my academic journey. I also acknowledge my brother Thamer, who stood by my side despite the physical distance from our home country. Special recognition goes to my husband Abdaelalah for his unwavering support, patience, and belief in my capabilities. Also, This journey would not have been as

meaningful without the warmth and joy that my baby Misk brings to our family.

I extend my thanks to my peers in the Electronic Structure Group, for their camaraderie and collaboration. Our shared experiences have enriched my research journey. I also want to acknowledge the Computational Physics Group, with a special mention to Mrwah. Our ability to exchange ideas, engage in insightful discussions, and enjoy academic exploration together has been a highlight of my time in the group.

To everyone mentioned and countless others contributing to my academic and personal growth, I express my sincere gratitude for being integral to this transformative chapter in my life.

A dedication to my Father, Ali Shafei

CHAPTER 1

INTRODUCTION AND BACKGROUND

Computational science, an interdisciplinary field that acts as a crucial link between scientific exploration and technological progress, has emerged as a dynamic force. By harnessing the immense computational power of computers and employing sophisticated algorithms, this field enables scientists to simulate, analyze, and forecast intricate natural phenomena across diverse scientific domains. Amongst these domains lies the study of clay materials.

Clay minerals have recently gained attention due to their numerous desirable properties, such as mechanical strength, optical absorption, and cation exchange capacity. Studying the structure and composition of clay minerals is expected to grow in the near future due to the discovery of new applications and refinement of existing ones [59, 72]. This is particularly relevant for applications that require barriers for water movement, such as earthen dams, leaks in ponds, and toxic waste landfills [36]. Furthermore, there is a recent and fascinating application in the field of spectroscopy[25]. Clay minerals are small crystalline granules that occur during the formation process of silicate-bearing rocks. They can make up to 40% of the minerals in sedimentary rocks and are a substantial part of soil. Additionally, they are commonly classified as hydrous layer aluminum phyllosilicate particles

with size less than 2μm[32, 7]. Moreover, they have highly reactive surfaces capable of altering soil properties [18]. Clay minerals have always been of great interest to researchers, particularly in the interrelated disciplines of physics, chemistry, and earth sciences. A comprehensive understanding of their composition and physical characteristics is crucial to comprehend fundamental aspects, such as bond strength, solvation effect, spectral characterization, optical absorption, elasticity, and seismic wave velocities. This requires a thorough understanding of the atomistic composition, electronic structure, interatomic bonding, charge transfer, optical properties, and mechanical properties of these minerals. Even though clay minerals have been the subject of extensive experimental research, they still lack detailed understanding of their structure and characteristics, particularly when it comes to atomic bonding, density of states (DOS), and mechanical properties [74].

In this dissertation, we embark on an intriguing journey where computational science converges with clay material studies.

1.1 Outline of Dissertation

This dissertation is organized as follows. The second chapter focuses on the background theory of the methodology. The third chapter is a comparative study between Kaolinite, Muscovite, and Montmorillonite, which is reprinted (adapted) with permission from (Layla Shafei, Puja Adhikari, and

Wai-Yim Ching. "DFT Study of Electronic Structure and Optical Properties of Kaolinite, Muscovite, and Montmorillonite" Crystals Journal 2021, 11(6), 618 Copyright (2021) by the authors. Licensee MDPI, Basel, Switzerland. Chapter 4 is a study of salvated Montmorillonite clay structure using a large scale which is reprinted with permission from (Layla Shafei, Puja Adhikari, Saro San, and Wai-Yim Ching. "Electronic Structure and Mechanical Properties of Solvated Montmorillonite Clay using Large-Scale DFT Method." Crystals Journal 2023, 13(7), 1120; Copyright 2023 by the authors. Licensee MDPI, Basel, Switzerland. It is an open-access article distributed under the terms and conditions of the Creative Commons Attribution (CC BY) license (https:// creativecommons.org/licenses/by/ 4.0/). Chapter 5 concludes the research with final remarks and recommendations.

CHAPTER 2

THEORY AND METHODOLOGY

In this dissertation, we used first-principles methods based on Density Functional Theory (DFT) to explore electronic structure, interatomic bonding of materials, optimization, and mechanical properties. Even though DFT calculations are conducted at the atomic level, they are capable of providing accurate and realistic predictions of material properties that are in line with experimental values. In order to create new materials and improve their qualities, computational technologies are essential. An overview of the fundamental concepts of reputable first-principles approaches will be given in this chapter. It will next go into detail about the computational approaches used in this work, which include the Vienna ab initio simulation package (VASP) [77] and the orthogonalized linear combination of atomic orbitals (OLCAO) package [10, 11]. These two computational packages were utilized in our research.

2.1 Density Functional Theory

Density Functional Theory (DFT) is widely employed in the fields of computational chemistry and condensed matter physics, thanks to its reasonable accuracy, scalability, and computational efficiency. DFT is utilized for the

atomic-level calculation of a material's electronic structure, resolving intricate N-electron wave functions through the electron density approach[63]. This method essentially treats a many-electron system as a functional of the ground-state electron density, aiding in the solution of the Schrödinger equation and the description of various material properties, including those of complex materials. By simplifying the many-body wave function problem and reducing it to the ground-state electronic density, DFT finds extensive application in diverse scientific disciplines, encompassing physics, chemistry, biology, materials engineering, and mineralogy.

The foundation of DFT is built upon the Hohenberg and Kohn $\mathrm{H}-\mathrm{K}$ [30]. The first $\mathrm{H}-\mathrm{K}$ theorem states that the ground-state electron density $\rho(r)$ uniquely determines the ground-state energy and the external potential $V_{ext}(r)$ of a quantum system. The energy of the ground state for any system subjected to an external potential $V_{ext}(r)$,the expression for the function of the electron density $\rho(r)$ as follows:

$$E_V[\rho(r)] = \int \rho(r) V_{ext}(r) dr + F_{\mathrm{HK}}[\rho(r)] \tag{2.1}$$

where F_{HK} represents a universal functional of an electron density distribution in a physical system $\rho(r)$. This universal functional, denoted as F_{HK}, is the sum of two important components: the kinetic energy functional $T[\rho(r)]$ and the electron-electron interaction functional $V_{ee}[\rho(r)].F_{\mathrm{HK}}[\rho(r)]$ is known

as a universal function because it can be used to describe the behavior of electrons in any physical system, regardless of the external potential $V_{\text{ext}}(r)$ acting on the system. As a result, the expression for $F_{\text{HK}}[\rho(r)]$ can be written as follows:

$$F_{\text{HK}}[\rho(r)] = T[\rho(r)] + V_{ee}[\rho(r)] \tag{2.2}$$

where,

$$T[\rho(r)] = \left\langle \psi_0 | \hat{T} | \psi_0 \right\rangle \tag{2.3}$$

and

$$V_{ee}[\rho(r)] = \left\langle \psi_0 | \hat{V_{ee}} | \psi_0 \right\rangle \tag{2.4}$$

$V_{ee}[\rho(r)]$ can be simplified as follows:

$$V_{ee}[\rho(r)] = J[\rho(r)] + E_{ncl}[\rho(r)] \tag{2.5}$$

with

$$J[\rho(r)] = \frac{1}{2} \iint \frac{\rho(r)\rho\left(r'\right)}{|r - r'|} dr dr' \tag{2.6}$$

$J[\rho(r)]$ refers to the classical Coulomb repulsion component in equation (2.5), while E_{ncl} denotes a non-classical term contributing to electron-electron interaction, which is the central aspect of "exchange-correlation energy". This elusive but critical quantity is important in describing electronic interactions in the system.

The second H-K theorem establishes a connection between the system's electron density and the minimal ground state energy. "The energy functional $E_V[\rho(r)]$ attains its minimum value, representing the ground state energy E_0 when calculated for the correct ground-state electron density $\rho_0(r)$" i.e

$$E_0 = \int \rho_0(r) V_{ext}(r) dr \tag{2.7}$$

The solution to the equation (2.1) remains elusive until $F_{\mathrm{HK}}\ [\rho(r)]$ is known. Additionally, the functionals $E_{ncl}[\rho(r)]$ and $T[\rho(r)]$ lack precise definitions. This necessitates the application of DFT to address complex problems involving many electrons, particularly due to the intractable nature of the quantity $F_{\mathrm{HK}}\ [\rho(r)]$. Minimizing the functional of the three-dimensional density function within the given external potential aids in determining the precise form of $F_{\mathrm{HK}}\ [\rho(r)]$for the electron density $\rho(r)$. Since the H-K theorem doesn't offer a direct solution for the functional$F_{\mathrm{HK}}\ [\rho(r)]$, Kohn and Sham (K-S) devised a method to find $E_V[\rho(r)]$ by solving the equation for the electron density $\rho(r)$, capable of yielding an unknown functional used in approximation. According to Kohn and Sham (K-S), the kinetic energy of a really interacting reference system with the density of a non-interacting reference can be stated as:

$$T = -\frac{1}{2} \sum_{i=1}^{N} \langle \Psi_i | \nabla^2 | \Psi_i \rangle \tag{2.8}$$

In this context, the kinetic energy T_s differs from the actual kinetic energy of the genuinely interacting system. Expressed in terms of T_s, $F_{\mathrm{HK}}[\rho(r)]$ can be formulated as:

$$F[\rho(r)] = T_s[\rho(r)] + J[\rho(r)] + E_{\mathrm{XC}}[\rho(r)] \tag{2.9}$$

The solution to equations (2.2) and (2.9) is as follows:

$$E_{XC}[\rho(r)] = [T[\rho(r)] - T_s[\rho(r)]] + [V_{ee}[\rho(r)] - J[\rho(r)]] \tag{2.10}$$

Utilizing equation (2.5), equation (2.9) transforms to:

$$E_{XC}[\rho(r)] = [T[\rho(r)] - T_s[\rho(r)]] + E_{ncl}[\rho(r)] \tag{2.11}$$

$$E_{XC}[\rho(r)] = T_R[\rho(r)] + E_{ncl}[\rho(r)] \tag{2.12}$$

The first term of equation (2.12) $T_R[\rho(r)]$ represents the residual part of the true kinetic energy, excluding the non-interacting system. Here, $E_{XC}[\rho(r)]$ is the exchange-correlation energy functional, encompassing the residual part of the true kinetic energy, the non-classical contribution of self-interaction, and the effects of exchange and correlation in potential energy.

The energy functional for a real interacting system is constructed by

utilizing equations (2.1) and (2.9), which:

$$E_V[\rho(r)] = \int \rho(r)V_{ext}(r)dr + T_s[\rho(r)] + J[\rho(r)] + E_{XC}[\rho(r)] \tag{2.13}$$

In the case of a non-interacting system, the energy expression consists solely of two components: the kinetic energy, denoted as KET_s, and the energy resulting from the interaction with the external potential $V_{ext}(r)$. Thus, we can express it as:

$$E_V[\rho(r)] = \int \rho(r)V_{ext}(r)dr + T_s[\rho(r)] \tag{2.14}$$

The equation (2.14) can be minimized without any conditions. To create a conditional minimum problem, we introduce a functional $G[\rho(r)]$ as:

$$G[\rho(r)] = E_V[\rho(r)] - \frac{\lambda}{2}\int |\rho(r)|^2 dr \tag{2.15}$$

Where λ represents the Lagrange multiplier associated with constraints. Referring to equations (2.14) and (2.15), we obtain:

$$G[\rho(r)] = \int \rho(r)V_{ext}(r)dr + T_s[\rho(r)] - \frac{\lambda}{2}\int |\rho(r)|^2 dr \tag{2.16}$$

The principle of stationary for the ground-state density provides

$$\delta \left\{ E_V[\rho(r)] - \lambda \left[\int \rho(r) dr - N \right] \right\} = 0 \tag{2.17}$$

By solving equation (2.17), we obtain:

$$\lambda = \frac{\delta E_Y[\rho(r)]}{\delta \rho(r)} \tag{2.18}$$

Equations (2.13) and (2.18) yield:

$$\lambda = V_{ext}(r) + \frac{\delta T_s[\rho(r)]}{\delta \rho(r)} + \int \frac{\rho(r')}{|r - r'|} dr' + V_{XC}(r) \tag{2.19}$$

$$\lambda = V_{eff}(r) + \frac{\delta T_s[\rho(r)]}{\delta \rho(r)} \tag{2.20}$$

$$V_{eff}(r) = V_{ext}(r) + \int \frac{\rho(r')}{|r - r'|} dr' + V_{XC}(r) \tag{2.21}$$

The exchange-correlation potential, commonly denoted as K-S potential, is determined as the functional derivative of the exchange-correlation energy E_{XC} with respect to the electron density$\rho(r)$:

$$V_{XC}(r) = \frac{\delta E_{XC}[\rho(r)]}{\rho(r)} \tag{2.22}$$

By solving the one-electron Schrödinger equation for a given $V_{eff}(r)$, we can obtain the electron density $\rho(r)$ that satisfies:

$$\left[-\frac{1}{2}\nabla^2 + V_{eff}(r)\right]\psi_i(r) = \varepsilon_i\psi_i(r) \tag{2.23}$$

The solution obtained from equation (2.23), represented by the value of the wave function $\psi_i(r)$, is utilized in determining the electron density:

$$\rho(r) = \sum_{i=1}^{N} |\Psi_i|^2 \tag{2.24}$$

The K-S equations, encapsulated in Equations (2.21) to (2.24), form the foundation of the K-S approach. Initiated with an initial estimate of the electron density, the effective potential is computed, and the K-S equation is iteratively solved. Subsequently, the electron density $\rho(r)$ is recalculated. This iterative process continues until self-consistency is achieved, upon which quantities such as force and energy are computed. If self-consistency is not attained, the effective potential is recalculated, and the process is reiterated.

Despite the exactness of the K-S approach, the presence of the indeterminate exchange-correlation functional (E_{XC}) poses challenges in solving the equations. The determination of this functional remains a focal point even in contemporary Density Functional Theory (DFT). The exchange-correlation energy E_{XC} arises from the interaction among electrons, influenced by the

Coulomb interaction and their quantum numbers. E_{XC} can be decomposed into exchange and correlation components. The exchange interaction arises from the Pauli exclusion principle, which dictates that two electrons occupying the same region cannot possess identical sets of four quantum numbers. The correlation energy arises from the correlated movement of electrons with opposite spins. One commonly employed approximation for solving the exchange-correlation functional is the local density approximation (LDA). In LDA, the density at a specific point r is utilized to calculate the exchange-correlation energy at that point. The LDA expression is given by:

$$E_{XC}[\rho(r)] = \int \rho(r)\epsilon_{XC}[\rho(r)]dr \tag{2.25}$$

Here, ϵ_{XC} represents the exchange-correlation energy of an electron in a homogeneous electron gas with density $\rho(r)$. LDA, being simple, accurate, and computationally economical, is extensively employed in solid-state physics for describing the ground-state properties of many-electron systems.

However, when dealing with rapidly varying densities, LDA may need correction. LDA assumes uniform density at a point r, but real systems often exhibit spatial non-uniformity. In such cases, the spatial variation of electron density must be considered in the exchange-correlation energy functional. This leads to the formulation of the generalized gradient approximation (GGA) expressed as:

$$E_{XC}^{GGA}[\rho(r)] = \int f(\rho(r), \nabla\rho(r))dr \tag{2.26}$$

where the integral is a function of the local density $\rho(r)$ and its gradient. Equation (2.26) represents a generalized gradient approximation (GGA), and various GGAs, such as PBE by Perdew, Burke, and Ernzerhof[64], B3LYP by Becke's three-parameter hybrid method[5], and Lee, Yang, and Parr[43], exist. The choice between PBE and B3LYP often depends on the discipline, with PBE being more prevalent in Physics and B3LYP in Chemistry. Further details on the computational packages VASP and OLCAO will be elaborated in subsequent sections.

2.2 Vienna Ab Initio Simulation Package (VASP)

VASP, developed by Kresse and colleagues in 1993[38, 39], stands as a prominent quantum mechanical computational package. Widely acclaimed for first principles and ab initio molecular dynamics calculations, VASP finds extensive use in exploring electronic structure and dynamic properties, particularly in the realms of condensed matter physics and material engineering.

VASP exhibits remarkable flexibility in computational capabilities, employing various approaches to solve the Schrödinger equation, including the Density Functional Theory (DFT) method using the Kohn-Sham (K-S) equation, the Hartree-Fock (H-F) approximation with Green functions using the

Roothaan equation, hybrid functionals combining H-F with DFT, and many-body perturbation theory.

To efficiently handle wavefunction operations between real and reciprocal space, VASP employs a plane-wave basis set, implemented through two techniques: the projector augmented wave (PAW) method[42, 6] and the ultra-soft pseudo-potential method[83, 40]. While the PAW method is more accurate, it comes at the expense of increased computational time.

The challenge of solving the all-electron plane wave is practically mitigated by using pseudopotential approximations, focusing on chemical bond formation regions and ignoring some core level nodal features. VASP employs three types of potentials: norm-conserving pseudopotential[41], ultra-soft Vanderbilt pseudopotential[83, 40], and PAW[42, 6]. This study adopts the PAW-PBE method[65], known for its accuracy within the Generalized Gradient Approximation (GGA) in VASP.

For calculations of the self-consistency cycle (SCF), VASP allows iterative matrix diagonalization methods like the conjugate gradient scheme[8], blocked Davidson algorithm[14], and residual minimization with direct inversion of the iterative subspace (RMM-DIIS)[89, 26]. This study efficiently employs RMM-DIIS and blocked Davidson for matrix diagonalization, utilizing the stability of the blocked Davidson algorithm and the speed of RMM-DIIS in a combined approach. Efficient charge density mixing in VASP is achieved

through the Broyden and Pulay mixing scheme[67, 34].

VASP's parallelization enhances its efficiency for parallel calculations, enabling the analysis of larger systems with several hundred or 1000 atoms. Within the scope of this study, VASP is utilized for the purpose of optimizing the geometry of the system, in addition to assessing its mechanical and elastic properties.

2.3 Geometry Relaxation

The relaxation of material structures through geometric adjustments is a critical precursor for in-depth property analysis. To comprehensively evaluate the desired properties of a system, it is crucial to establish a realistic and nearly perfect structural model initially. The structure obtained through Density Functional Theory (DFT) optimization often diverges from the experimental structure, particularly in lattice characteristics. Therefore, the initial geometric relaxation serves as a fundamental step for the subsequent analysis of properties. VASP is primarily composed of four input files INCAR, KPOINTS, POSCAR, and POTCAR essential for simulating any system. The INCAR file governs calculation parameters, the KPOINTS file specifies the number of K-points based on the system size, the POSCAR file contains initial position and lattice vector information, and the POTCAR file consolidates potential information for all atoms in the same order as outlined

in the POSCAR file.

2.4 Elastic and Mechanical Properties Calculation

The assessment of a material's elastic and mechanical properties is crucial for its various applications. Advances and refinements in computational methods have significantly enhanced the precision of ab initio calculations for these properties. Typically, two approaches are employed in ab initio calculations of mechanical properties.

The first method is to analyze the total energy of a crystal as a function of volume or pressure:

$$E(V, \varepsilon) = E(V_0) + V \sum_{i=1} \sigma_i \varepsilon_i + \frac{V}{2} \sum_{ij} C_{ij} \varepsilon_i \varepsilon_j + \dots \tag{2.27}$$

ε_i denotes strain components, σ_i stress components, and C_{ij} elastic tensors. The total energies obtained for different strains are fitted to a parabola near the minimum energy, facilitating the derivation[75] of elastic constants.

The second approach employs the ab initio stress-strain relationship defined by the Nielsen and Martin scheme[61]. Hooke's law can be solved by applying a small strain ε to a fully relaxed system:

$$\sigma_i = \sum_{j=1} C_{ij} \varepsilon_j \tag{2.28}$$

The stress components σ_i here exhibit linear dependence on the applied strain ε_j. By solving this equation, the values of elastic tensors C_{ij} and their inverse compliance tensors S_{ij} can be obtained. Bulk mechanical parameters are then evaluated using these values, along with the Voigt-Reuss-Hill approximation for polycrystals[85, 29, 70]. The upper limit of the bulk modulus K_{Voight} and the shear modulus G_{Voight} are given by Voigth's method, and the lower limit o of bulk modulus K_{Reuss} and shear modulus G_{Reuss} is given by Reuss's approximation.

$$K_{\text{Voigt}} = \frac{1}{9}(C_{11} + C_{22} + C_{33}) + \frac{2}{9}(C_{12} + C_{13} + C_{23}) \tag{2.29}$$

$$G_{\text{Voigt}} = \frac{1}{15}(C_{11} + C_{22} + C_{33} - C_{12} - C_{13} - C_{23}) + \frac{1}{5}(C_{44} + C_{55} + C_{66}) \tag{2.30}$$

$$K_{\text{Reuss}} = \frac{1}{(S_{11} + S_{22} + S_{33}) + 2(S_{12} + S_{13} + S_{23})} \tag{2.31}$$

$$G_{\text{Reuss}} = \frac{15}{4(S_{11} + S_{22} + S_{33}) - 4(S_{12} + S_{13} + S_{23}) + 3(S_{44} + S_{55} + S_{66})} \tag{2.32}$$

Hill's approximation utilizes the average value of the Voigt and Reuss approaches, yielding bulk modulus (K) and shear modulus (G) values.

$$K = \frac{K_{\text{Voigt}} + K_{\text{Reuss}}}{2} \tag{2.33}$$

$$G = \frac{G_{\text{Voigt}} + G_{\text{Reuss}}}{2} \tag{2.34}$$

Based on the values of K and G, Young's modulus (E) and Poisson's ratio (η) can be determined in the following :

$$E = \frac{9KG}{3K + G} \tag{2.35}$$

$$\eta = \frac{3K - 2G}{2(3K + G)} \tag{2.36}$$

2.5 Orthogonalized Linear Combination of Atomic Orbitals (OLCAO)

In the analysis of VASP simulated structures, OLCAO is employed to assess electronic structure and optical properties. Developed by Professor Ching, the OLCAO package is an in-house tool systematically refined for the study of complex electronic structures. The amalgamation of VASP and OLCAO presents an optimal blend, balancing accuracy, efficiency, and cost-effectiveness, making it a preferred choice for exploring various complex systems. OLCAO is utilized to compute electronic structure, interatomic bonding, partial charge, and optical properties of simulated models. OLCAO is a method that considers all- electrons in its calculations and functions based on the Local Density Approximation (LDA) within Density Functional

Theory (DFT). It employs atomic orbitals for basis expansion, providing flexibility with minimum basis (MB), full basis (FB), and extended basis (EB) sets. This flexibility is particularly advantageous in electronic structure calculations for materials of varying characteristics and dimensions. OLCAO, coupled with VASP, has demonstrated success in studying large biological systems[3, 33, 66],liquids[4, 46],and amorphous solids[90, 44, 86].

The OLCAO method is an extension of the traditional LCAO method, utilizing solid-state wave functions $\Psi_{nk}(r)$ in atomic orbitals with Bloch functions. It involves Gaussian Type Orbitals (GTO) and spherical harmonics associated with the angular momentum quantum number, expressed as

$$\Psi_{nk}(r) = \sum_{i.\gamma} C^{n}_{i\gamma}(k) b_{i\gamma}(k, r) \tag{2.37}$$

The band index (n) represents the orbital quantum number (i), while γ represents the atom's serial number. The Bloch sum ($b_{i.\gamma}(k, r)$) can be formed of:

$$b_{i\gamma}(k, r) = \frac{1}{\sqrt{N}} \sum_{v} e^{i(k \cdot R_v)} u_i(r - R_v - t_\gamma) \tag{2.38}$$

where R_v indicates the lattice vector, and t_γ represents the position of the $\gamma^t h$ atom in the cell. Also $u_i(r)$ indicates the linear combination of atomic orbitals which includes both radial and angular components, represented as:

$$u_i(r) = [\sum_{j=1}^{N} A_j r^l e^{(-\alpha_j r^2)}] Y_l^m(\theta, \phi) \tag{2.39}$$

The symbol i denotes the principal quantum number$n$, as well as the angular momentum quantum numbers(l, m). The parameter N indicates the number of Gaussian Type Orbitals (GTOs), while α_j is a set of predefined variables based on previous experiences. The values of α_j are in the geometric series $\alpha_{\min}$ to $\alpha_{\max}$.

The initial term,$\sum_{j=1}^{N} A_j r^l e^{(-\alpha_j r^2)}$, contributes to the radial aspect of the equation and signifies a linear combination of GTO. The utilization of GTO is advantageous since the product of two GTOs results in a new GTO, simplifying the evaluation of orbital interaction integrals. This simplification streamlines the mathematical processes of integration and differentiation. The subsequent term $Y_l^m(\theta, \phi)$ pertains to the angular component, comprising real spherical harmonics.

The set of atomic orbitals, denoted as $u_i(r)$ in Equation (2.39), encompasses core, occupied valence, and additional unoccupied orbitals. Depending on the material's nature and the system's dimensions, three types of basis sets—MB (Minimum Basis), FB (Full Basis), and EB (Extended Basis)—are chosen. The MB set, involving only core and valence shell orbitals, is particularly suitable for large amorphous systems. Conversely, FB set, which encompasses the MB plus empty orbitals from the next unoccupied shells,

is adequate for smaller systems to yield accurate results. For calculations involving spectral properties, where unoccupied states of higher energy are of interest, an additional level of unoccupied orbitals is incorporated into the FB set to create an EB set. This flexibility in selecting an atomic basis set allows for a balance between accuracy and computational time in OLCAO. OLCAO constructs its potential based on LDA of DFT. It follows an iterative process to solve the K-S equation for a single electron, with all quantities given in atomic units.

$$[-\nabla^2 + V_{e-n}(r) + V_{e-e}(r) + V_{xc}[\rho(r)]]\Psi_{nk}(r) = E_n(k)\Psi_{nk}(r) \qquad (2.40)$$

Where $-\nabla^2$ represents the kinetic energy. while V_{e-n} is the electron-nuclear, V_{e-e} is electron-electron Coulomb, and $V_{xc}[\rho(r)]]$ is exchange-correlation part of potential energy. The $V_{xc}[\rho(r)]]$ depends on electron density $\rho(r)$ which defined as $\rho(r) = \sum_{occ} |\Psi_{nk}(r)|^2$,which allows the above equation to be solved in a self-consistent consistently.

In the context of Density Functional Theory (DFT) and the Local Density Approximation (LDA), the exchange and correlation components of the potentialV_{xc} are essential in explaining the complex dynamics of many-electron interactions. The exchange-correlation functional ε_{xc}, a mathematical construct that depends on the electron density and captures the complex exchange-correlation energy$E_{xc}(r)$, is the source of these intricately derived

components. The following is the mathematical expression for this energy:

$$E_{xc}(r) = (r) \int \rho(r)\varepsilon_{xc}[\rho(r)]\, dr \tag{2.41}$$

This expression can be further elucidated:

$$V_{xc}(r) = \frac{d(\rho\varepsilon_{xc}[\rho])}{d\rho} = -\frac{3}{2}\alpha \left[\frac{3}{\pi}\rho(r)\right]^{1/3} \tag{2.42}$$

In the context of OLCAO under LDA, the total energy (E_T) of the system is formulated as:

$$E_T = \sum_{n,k}^{occ} E_n(k) + \int \rho(r) \left(\varepsilon_{xc} - V_{xc} - \frac{V_{e-e}}{2}\right) dr + \frac{1}{2}\sum_{\gamma,\delta} \frac{Z_\gamma Z_\delta}{R_\gamma - R_\delta} \tag{2.43}$$

The initial term signifies the aggregation over one-electron states, while the ultimate term pertains to the summation over the lattice. The incorporation of a factor of $\frac{1}{2}$ is implemented to rectify the double-counting issue associated with Coulomb potential. The total energy assumes paramount importance as a fundamental physical parameter within the framework of OLCAO, playing a pivotal role as a criterion for achieving energy convergence in the self-consistent potential.

The OLCAO method is well-suited for computing a wide range of electronic properties, including band structure, density of states, bond order, effective charge, dielectric function, and optical properties. The evaluation

of effective charge enables a thorough examination of charge transfer phenomena within the system. The effective charge (Q^*) is the number of electronic charges associated with an atom calculated using the Mulliken scheme[58, 57, 56]. In the Mulliken scheme, the partial charge associated with the i-th orbital of the α-th atom in the normalized state is defined as:

$$\sum_{i,\alpha}^{n} \rho_{i,\alpha}^{n} = \int |\Phi_n(r)|^2 \, dr = 1 \tag{2.44}$$

$$\rho_{i,\alpha}^{n} = \sum_{j,\beta} C_{i\alpha}^{n^*} C_{j\beta}^{n} S_{i\alpha,j\beta} \tag{2.45}$$

Here n denotes the band index, and i and j represent the orbital quantum numbers of atoms α,β respectively. $S_{i\alpha,j\beta}$ are the overlap integrals between the i^{th} orbital in the α^{th} atom and j^{th} orbital in the β^{th} atom. The $C_{j\beta}^{n}$ are eigenvector coefficients of the n^{th} band and j^{th} orbital in the β^{th}atom.

The density of states (DOS), denoted as $G(E)$, provides the count of electron states per unit energy in the material. It is expressed as:

$$G(E) = \frac{\Omega}{(2\pi)^3} \frac{d}{dE} \int_{BZ} dk = \frac{\Omega}{(2\pi)^3} \int (\frac{dS}{|\nabla E|}) \tag{2.46}$$

where Ω represents the volume of the unit cell, S is the overlap matrix, and the integral is taken over the constant energy surface on the Brillouin Zone (BZ).

In the context of simulated crystals, the inter-band optical properties are elucidated through the frequency-dependent complex dielectric function$\varepsilon(h\omega) = \varepsilon_1(\hbar\omega)+i\varepsilon_2(\hbar\omega)$ The real and imaginary parts, $\varepsilon_1(\omega)$ and $\varepsilon_2(\omega)$, are obtained from the following equations:

$$\begin{aligned}\varepsilon_2(\hbar\omega) = \frac{e^2}{\pi m\omega^2}\int_{BZ} dk^3 \sum_{n.l} \left|\langle\psi_n(k,r)\left|-i\hbar\nabla\right|\psi_l(k,r)\rangle\right|^2 \\ \times f_l(k)\left[1-f_n(k)\right]\delta\left[E_n(k)-E_l(k)-\hbar\omega\right].\end{aligned} \tag{2.47}$$

$$\varepsilon_1(\hbar\omega) = 1 + \frac{2P}{\pi}\int_0^\infty \frac{s\varepsilon_2(\hbar\omega)}{s^2-\omega^2}ds \tag{2.48}$$

In the given context, where l denotes occupied states and n represents unoccupied states, the Fermi distribution functions $f_l(k)$ and $f_n(k)$ characterize the electron occupation probabilities. The refractive index n is then derived by taking the square root of ε_1 at zero frequency, expressed as $n = \sqrt{\varepsilon_1(0)}$. The subsequent computation of the energy loss function (ELF) $F(\omega)$ relies on the imaginary part of $(1/\varepsilon)$.

$$F(\omega) = IM\left(-\frac{1}{\varepsilon(\omega)}\right) = \frac{\varepsilon_2(\omega)}{\varepsilon_1^2(\omega)+\varepsilon_2^2(\omega)} \tag{2.49}$$

CHAPTER 3

DFT STUDY OF ELECTRONIC STRUCTURE AND OPTICAL PROPERTIES OF KAOLINITE, MUSCOVITE, AND MONTMORILLONITE

3.1 Introduction

Ab initio computational research seems to be the most suitable way to get bonding information, total density of states (TDOS), partial density of states (PDOS), and mechanical properties due to recent developments in supercomputing technology, in contrast to the costly experimental trial-and-error approach in the laboratory. Some examples of clay minerals, for which the electronic structure and bonding information are kind of unknown and ripe for such investigation, include kaolinite, muscovite, and montmorillonite (MMT). Kaolinite, $Al_2Si_2O_5(OH)_4$, is one of the most common clay minerals. It comprises the principal ingredients of kaolin (china clay). The kaolin group includes nacrite, dickite, halloysite, and kaolinite. All of them have an identical chemical composition but in a different crystalline form. Kaolinite, a classification from the phyllosilicate group, is composed of alternating sheets of silicates and aluminum hydroxide, as shown in Figure 1. The lattice parameter, number of atoms, and space group of kaolinite is shown in Table

1. Studying kaolinite can aid in many important areas such as geology, agriculture, construction, and engineering applications [60]. Additionally, the world mining production of kaolin in 2016 was 37.0 Mt, making it the most mined clay [15]. Kaolinite is used in the adsorption of some heavy metals; furthermore, it is used to remove pollutants from water[92]. It is extensively used in the field of paper production, plastics, paints, adhesives, insecticides, medicines, food additives, bleach cement, fertilizers, cosmetics, crayons, pencils, detergents, paste, floor tiles, textiles, and many more [23]. One of the most important potential applications uses kaolinite in pharmaceutical applications, especially for cancer treatment[24]. Additionally, kaolinite has a much simpler crystal structure that is not easily decomposable and has been studied in different aspects, such as its fiber mechanical properties, kinetics of metal adsorption [53], and far more. However, to further improve its application, it is important to conduct a thorough study of the electronic and mechanical properties.

Muscovite, $KAl_2\left(Si_3Al\right)O_{10}(OH)_2$[45], consists of two tetrahedral sheets to one octahedral sheet, as shown in Figure 1. The lattice parameter, number of atoms, and space group of muscovite is shown in Table 1. Muscovite crystal has layered structures that enable nearly perfect cleavage that allows for the formation of a smooth surface at an atomic scale. Layer properties provide information on the surface interactions and related properties.

There have been only a few studies related to layering so far [87]. Muscovite is present in metamorphic, igneous, and sedimentary rocks, and is among the most common minerals of the mica family. It is slightly larger than clay minerals and has a platy shape similar to clay minerals. It can be easily identified by its bright silvery sparkle and used to add "glitter" to paints and cosmetics. Since it can resist electricity and heat, it is also used as an insulator in electrical appliances and in ovens. Moreover, its slightly transparent nature allows for its high usage in windows and other construction industries. Montmorillonite (MMT), $Al_2Si_4O_{10}(OH)_2$ [49], is a clay mineral of the smectite group that consists of two tetrahedral sheets to one octahedral sheet, as shown in Figure 1. The lattice parameter, number of atoms, and space group of MMT is shown in Table 1. Weathering of eruptive rock materials leads to the formation of MMT. It is capable of absorbing cations and is one of the most expandable clay minerals that can absorb a large quantity of water. Therefore, it can be used in numerous fields such as oil refining, pharmaceutical preparations, sugar refining, as a catalyst, and as a binder in many fields such as insulating materials. The major uses of MMT are as a sealant in many engineering applications, and as a barrier for landfills and toxic waste repositories [59]. In addition, montmorillonite is used to design polymer-clay nanocomposites, which are capable of changing their strength and resistance [82]. It can also form composites to biological entities such as

proteins and amino acids. Computational modeling may be the only venue that can provide useful information about this clay mineral with extremely complex structures. A deep analysis of the electronic structure in kaolinite, muscovite, and MMT can help to understand and modify clay minerals, which may significantly improve their surface properties and consequently increase their capacities and efficiencies in many applications, such as environmental cleanup applications [72]. This work presents a computational study of the structure and properties of these minerals. A fundamental understanding of the electronic structure and physical properties will have a broader impact on scientific advances in many frontiers. They range from medical applications such as kaolinite's use in cancer diagnosis and treatment and electrical applications, muscovite's use as an insulator and in engineering applications, and MMT's use as a sealant. Additionally, they can be used to improve cements, as data for seismic wave velocities for geoscience, and much more.

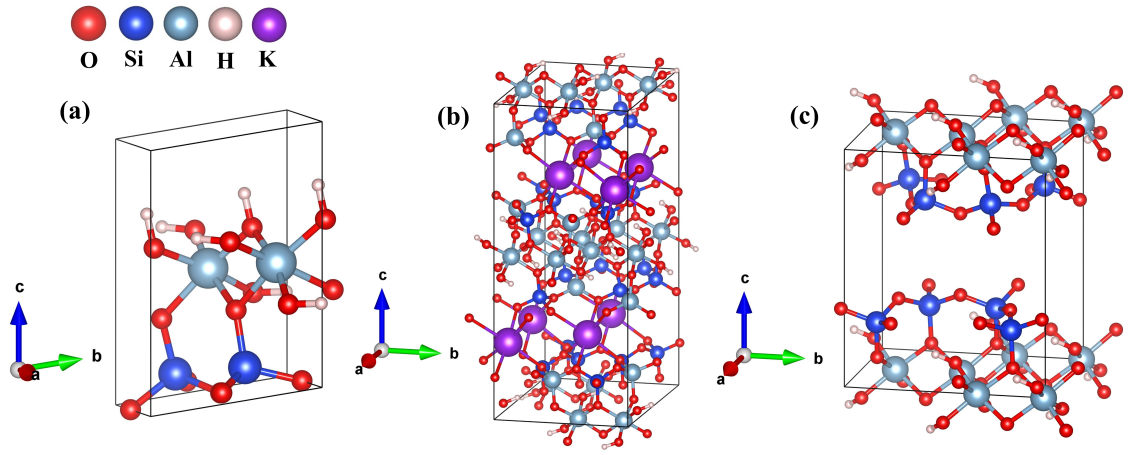

Figure 1: Shows ball and stick figures using Vesta [54] for (a) kaolinite, (b) muscovite, and (c) montmorillonite. The color used to represent the elements are shown in the top left side.

Table 1: The optimized lattice parameter, No of atoms, and space group of kaolinite, muscovite, and montmorillonite.

Crystal	Chemical Formula	No. Atoms (Space Group)	$a, b, c(\AA)$ α, β, γ
Kaolinite	$Al_2Si_2O_5(OH)_4$	17(P1)	$5.19, 5.18, 7.54$ $77.84°, 84.31°, 60.10°$ a. $5.15, 5.15, 7.41$ $75.14°, 84.12°, 60.18°$
Muscovite	$8\,[KAl_2\,(Si_3AlO_{10})\,(OH)_2]$	168(C12/c1)	$10.47, 9.10, 20.68$ $90°, 96.20°, 90°$ b. $5.19, 9.0020.10$ $90°, 95.18°, 90°$
MMT	$2\,[Al_2Si_4O_{10}(OH)_2]$	40(C121)	$5.21, 9.06, 10.27$ $90°, 99.46°, 90°$ c. $5.18, 8.97, 10.07$ $90°, 99.50°, 90°$

Unoptimized lattice parameters of a. kaolinite[28], b. muscovite [69], and c. montmorillonite [76]

3.2 Computation Methods

In this study, we used two computational packages, VASP and OLCAO. VASP is utilized for the optimization of the structures and for the calculation of elastic and mechanical properties as discussed in section 2.2 and section 2.4. A relatively high energy cutoff of 600eV, with electronic force convergence at 10^{-5}eV, was used. The KPOINTS used were $6\times6\times4, 2\times\ 2\times1$, and $2\times1\times1$ for kaolinite, muscovite, and MMT, respectively. We used the optimized structure obtained from VASP as input into OLCAO for the calculation of the electronic structure, interatomic bonding, and optical properties. We used a full basis (FB) for the self-consistent potential, total density of state (TDOS), partial DOS (PDOS), and band structure calculations. For the bond order (BO) calculation, we used a minimal basis (MB) based on the Mulliken scheme. A summation of all BOs of the crystal results in a total bond order (TBO), and by normalizing the TBO by the crystal's volume, the total bond order density (TBOD) is generated. TBOD is a single metric that can be used for the evaluation of the interior cohesion of a crystal and can be further divided into the partial bond order density (PBOD) for different types of bond pairs. For optical properties, we used an extended basis (EB), which includes a shell of unoccupied orbitals in addition to the FB. The effective charge Q^* and the partial charge (PC) for every atom in these systems were

obtained by using the following equation.

$$\Delta \mathrm{Q} = \mathrm{Q}_0 - \mathrm{Q}^* \tag{3.1}$$

For the calculation of the elastic and mechanical properties, a stress (σ_j) vs. strain (ε_i) response analysis [61, 91] scheme is applied to the fully relaxed structure to obtain the elastic coefficients $C_{ij}(i, j = 1, 2, 3, 4, 5, 6)$.

3.3 Results and Discussion

3.3.1 Electronic Structure

We obtained the atomic coordinates for kaolinite, muscovite, and MMT from Hess et al. [28], Radoslovich et al. [69], and Subramanian et al.[76], respectively. The calculated band structures of those three clay minerals' crystal structures are shown in Figure 2. The bandgap results clearly show that they are insulators. According to the calculations, the bandgaps of kaolinite, muscovite, and MMT were 4.84eV, 4.67eV, and 5.11eV, respectively. Our band gap results are consistent with a theoretical study [71] for kaolinite, which was 4.8eV. In addition, for the muscovite, our findings are following a DFT study [94] with values ranging from 3.96eV to 5.02eV, which is significantly lower than the experimental value of 7.85eV [13]. For MMT, our bandgap value was close to two other calculations, which were about 5.35eV

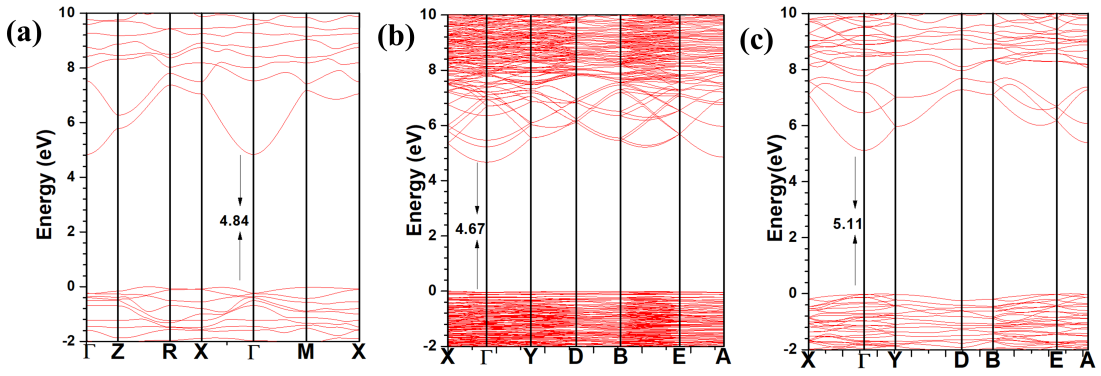

Figure 2: shows band structures for (a) kaolinite, (b) muscovite, and (c) montmorillonite. Muscovite and MMT show a direct bandgap whereas kaolinite shows an indirect bandgap.

[49] and 5.52eV [19]. All of them had a direct bandgap except for kaolinite. Among the three crystals, MMT had the widest bandgap.In muscovite, the bottom of the conduction band (CB) has a curvature whilst the top of the valence band (VB) is very flat. The calculated TDOS and further resolved PDOS for the three crystals in the energy range from -25eV to 25eV and are shown in Figure 3. The PDOS shows the relative contribution of each element to the TDOS, which helps to understand the bonding. Among the three crystals, kaolinite and MMT have same set of four elements, $\mathrm{H}, \mathrm{O}, \mathrm{Si}$, and Al. Besides these four elements, muscovite also consists of K, which was responsible for the sharp peak at energy -11eV, which was due to semi-core nature of the K-3p orbital. Most of the states and peaks in the TDOS for the three crystals were from O atoms. The states of $\mathrm{Al}, \mathrm{Si}, \mathrm{H}$, and K in the

same energy range with O atoms showed their bonding.

3.3.2 Interatomic Bonding

The interatomic interaction as BO vs. bond length (BL) distribution of these three crystals is shown in Figure 4. All of these three clay mineral crystals had $O-H, Si-O$, and $Al-O$, whereas $O-K$ bonding was only present in muscovite, as depicted in Figure 4 b. O-H bonds were the strongest bond in the three crystals, with a BO of 0.29e and a BL of around 0.94 A. Si- O bonds had a higher BO in muscovite at 0.30e and MMT at 0.29e, in comparison to kaolinite. Al-O bonds in muscovite were more scattered in comparison to kaolinite and MMT. In addition, there were some $O-H$ bonds in the range between 2.8 and 3.4$\dot{A}$, which represented hydrogen bonding. The PBOD and TBOD of these three crystals are shown in Table 2. The TBOD is the sum of the BO values of all bond pairs divided by the volume of the crystal. TBOD is a good parameter to gauge the internal cohesion in the system [16]. The TBOD values for these three crystals were similar. However, kaolinite was slightly more cohesive than MMT and muscovite. TBOD can be further resolved into PBOD to identify the impact of different bonding in the system. Si-O bonds had higher contribution, which was followed by $Al-O$ bonds in the three crystals. The $O-H$ bonds in muscovite and MMT showed the same $PBOD$ value of 0.003e/$\mathring{A}^3$ and a much lower value of 0.007e/$\mathring{A}^3$ in kaolinite.

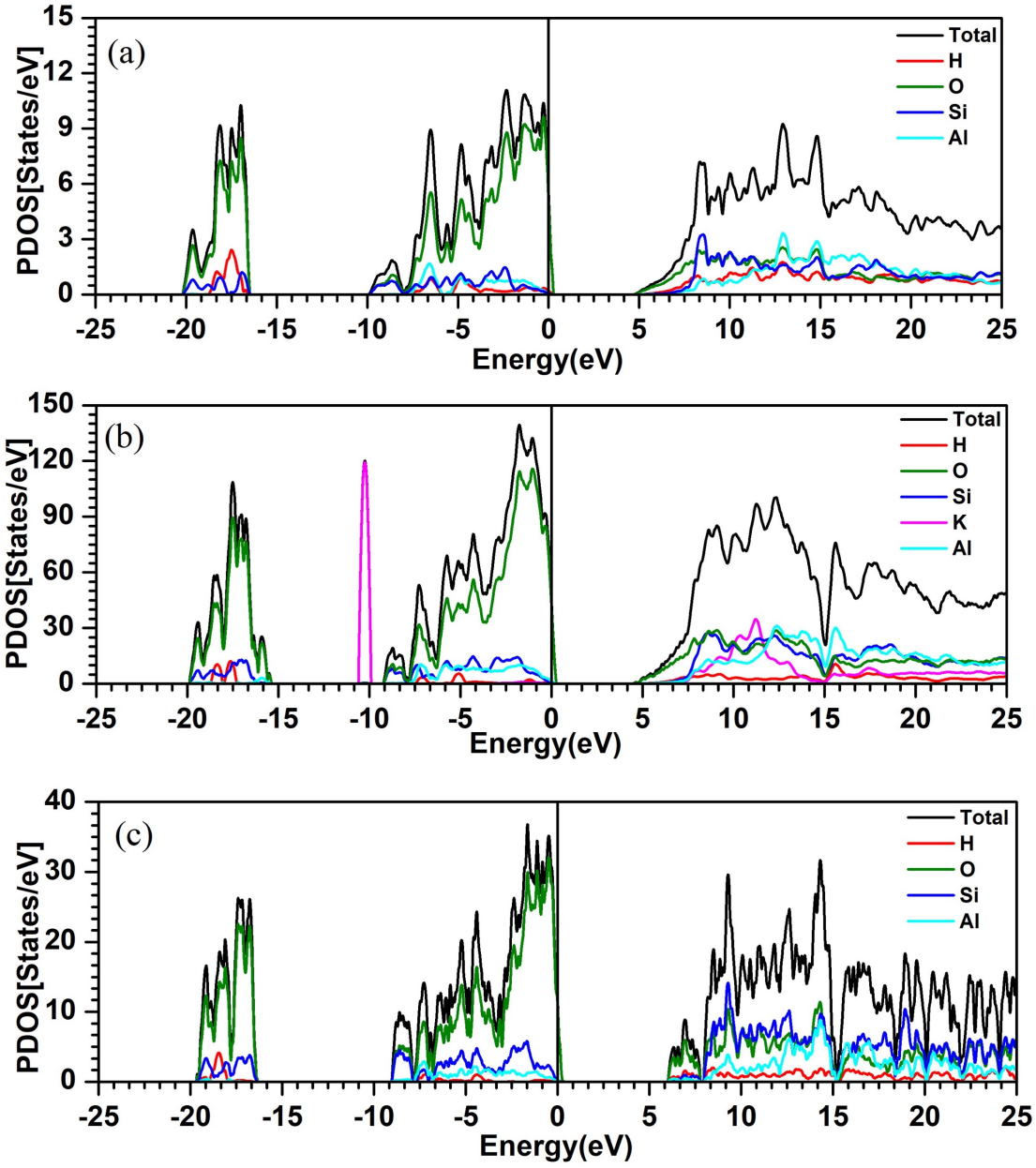

Figure 3: TDOS, PDOS of three clay minerals crystals for (a) kaolinite, (b) muscovite, and (c) montmorillonite.

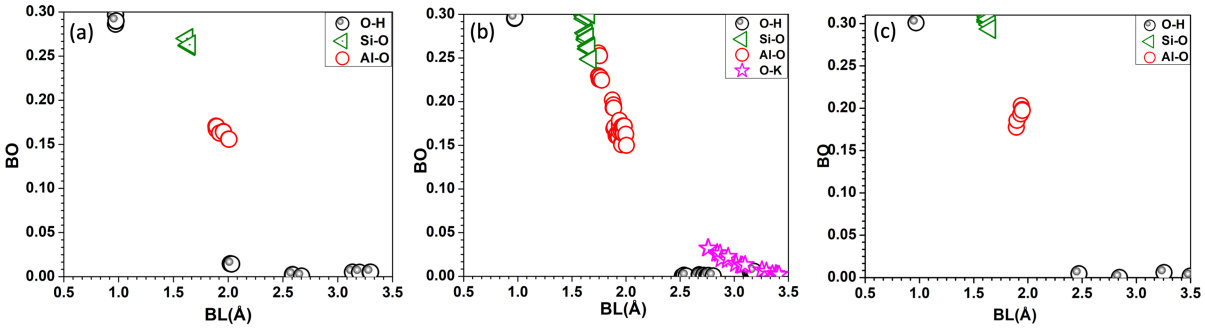

Figure 4: BOvs.BL of three clay minerals crystals for (a) kaolinite, (b) muscovite, and (c) montmorillonite.

Table 2: TBOD, and PBOD for kaolinite, muscovite and MMT

Crystal	Vol $(\mathring{A}^3)$	Bond	PBOD (electron/ $\mathring{A}^3$)	TBO	TBOD
Kaolinite	171.91	O-H	0.007		
		Si-O	0.013	5.446	0.032
		Al-O	0.012		
Muscovite	1957.66	O-H	0.003		
		Si-O	0.015		
		Al-O	0.013	57.096	0.031
		O-K	0.001		
		Al-H	0.000		
MMT	478.36	O-H	0.003		
		Si-O	0.019		
		Al-O	0.008	14.273	0.030

The PC of each atom is defined as the deviation of the effective charge from the neutral charge. The PC for every atom of the three crystals is shown in Figure 5. It is noted that had a negative PC in all three crystals

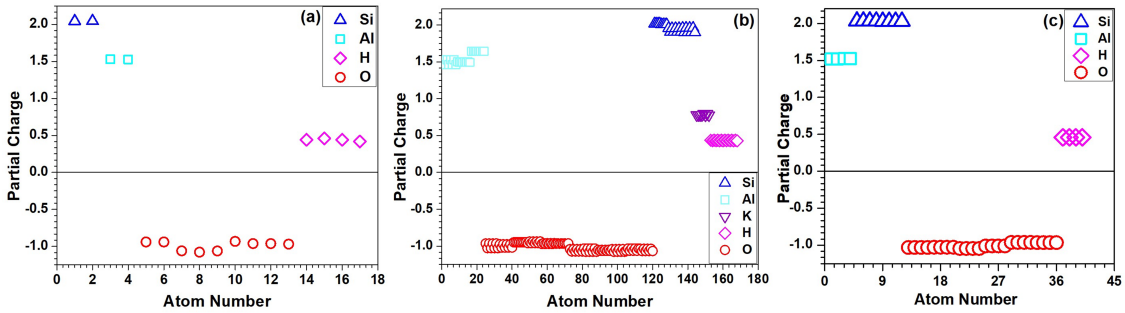

Figure 5: Distribution of partial charge ΔQ* for (a) kaolinite, (b) muscovite, and (c) montmorillonite.

and the other elements had a positive PC, as expected. It simply means that the oxygen gained more electrons from the other positively charged atoms. Minor variations in the PC of O, Al, and Si represent site variation.

3.3.3 Optical Properties

The optical behavior of the real (ε_1) and imaginary (ε_2) dielectric function of these three minerals is shown in Figure 6. We can obtain the static dielectric constant from the calculated dielectric functions by taking the zero-frequency limit of the real parts of the dielectric function. The refractive index (n) is calculated by taking the square root of $\varepsilon_1(0)$. The refractive indexes for kaolinite, muscovite, and MMT are 1.60, 1.58, and 1.52, respectively. Figure 6 presents the calculated energy-loss functions (ELF) for all three crystals. It shows the collective excitation of electrons at high frequency. The main peak of ELF is defined as the plasma frequency (ω_p).

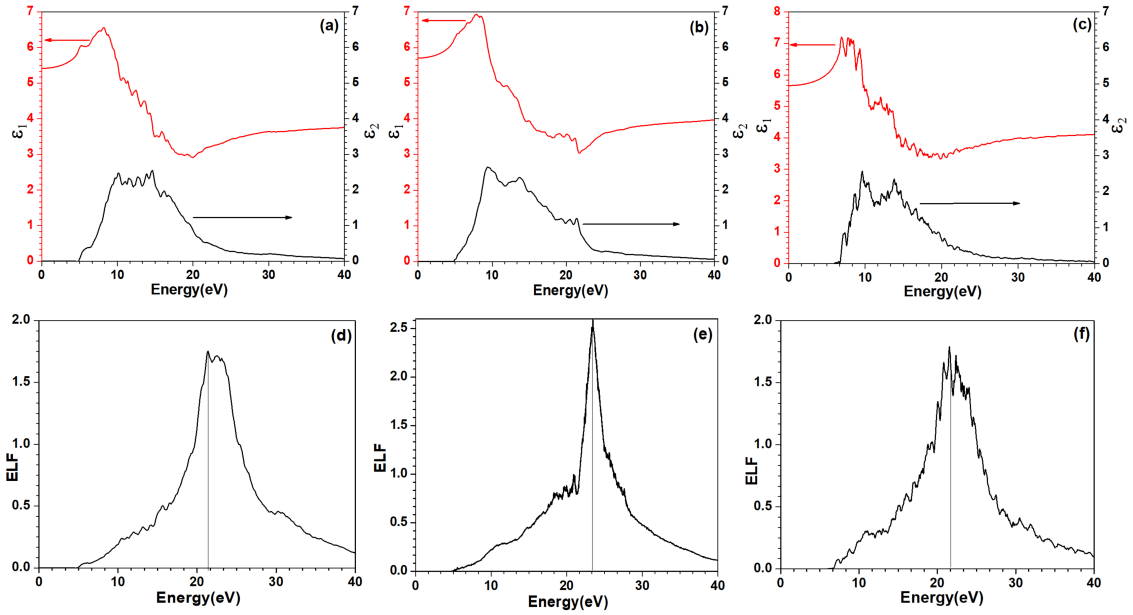

Figure 6: Optical dielectric function for the crystals from (a) kaolinite, (b) muscovite, and (c) montmorillonite. The black curve is for the real part (ε_1); the red curve is for the imaginary part (ε_2). (d-f) show the energy-loss function for kaolinite, muscovite, and montmorillonite, respectively.

Among the three crystals, muscovite had the highest ω_p at 23.59eV and kaolinite had lowest ω_{p} at 21.38eV.

3.3.4 Mechanical Properties

One of the important factors in clay mineral study is obtaining the elastic properties and the sound velocity, which will help to understand the seismic and sonic log [55]. We calculated the elastic coefficients from VASP relaxed structures for the three crystals. From the elastic coefficients, the mechanical parameters for these crystals were obtained. They were the bulk modulus

(K), shear modulus (G), Young's modulus (E), Poisson's ratio (η), Pugh's modulus ratio ($k = G/K$), and Vicker's hardness (Hv) and are summarized in Table 3. The calculated bulk modulus for kaolinite was 46.93 GPa, which falls in the experimentally obtained range of 21 to 55 GPa[84, 88]. The higher the bulk modulus, the less compressible the crystal is. The shear modulus represents the modulus of the rigidity of the material and Young's modulus represents the stiffness of the material. Among the three crystals, muscovite had the highest bulk modulus, Young's modulus, and shear modulus. Pugh's modulus ratio (G/K) estimates the brittleness or ductility of the material from comparative analysis. In Pugh's modulus ratio approximation, an empirical boundary value of 0.571 could be defined to classify metallic materials as brittle (> 0.571) or ductile (< 0.571) [79]. The calculated Pugh's modulus ratio (G/K ratio) for kaolinite, muscovite, and MMT was 0.678, 0.715, and 0.745, respectively. MMT is more brittle than kaolinite or muscovite. This could be a result of the difference in composition and structure. Vicker's hardness for the three crystals was calculated using Tian et al.'s [81] equation $\mathrm{H_V} = 0.92\mathrm{k}^{1.137}\mathrm{G}^{0.708}$. Muscovite had a higher Vicker's hardness in comparison to kaolinite and MMT (shown in Table 3). Young's modulus and shear modulus are further shown in a three-dimensional plot in Figure 7. The Young's modulus for the three crystals showed an anisotropic nature and the shear modulus showed a more complex nature, with both

translucent blue and green colors.

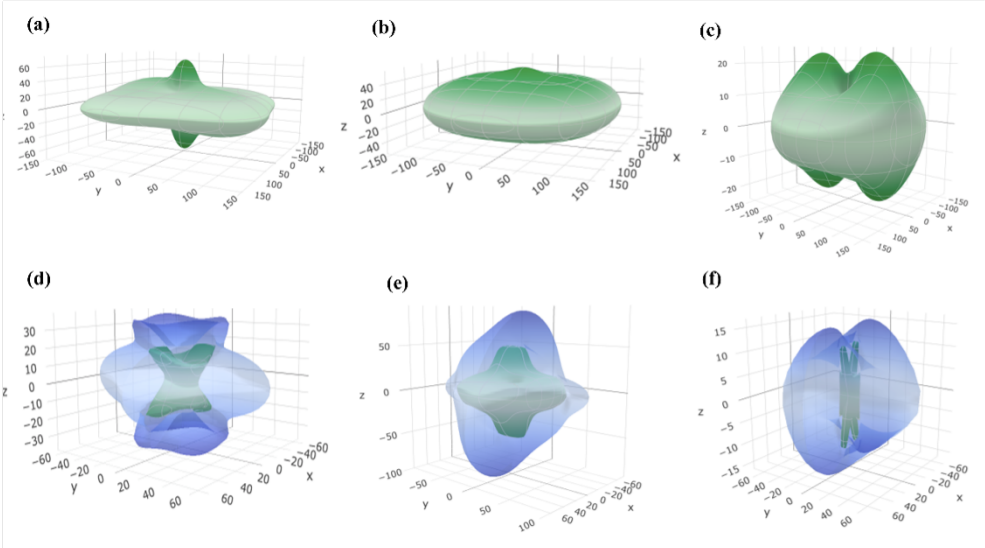

Figure 7: 3D representation surfaces of Young's modulus for (a) kaolinite, (b) muscovite, and (c) montmorillonite, (d-f) show Shear modulus for kaolinite, muscovite, and montmorillonite crystals respectively. Green: minimum positive, translucent blue: maximum positive[22].

Table 3: The calculated bulk modulus (K), shear modulus (G), Young's modulus (E), Poisson's ratio (η), Pugh's modulus ratio (k = G/K), and Vicker's hardness (HV) in GPa for kaolinite, muscovite, and MMT.

Crystal	K(GPa)	G(GPa)	E(GPa)	η	G/K	$H_V(GPa)$
Kaolinite	46.93	31.83	77.88	0.2235	0.6782	6.853
Muscovite	53.47	38.24	92.64	0.2112	0.7152	8.293
MMT	31.85	23.74	57.049	0.2015	0.7453	6.198

Once we obtained the elastic tensors for the three kaolinite, muscovite, and MMT minerals, it was also imperative to obtain the sound velocities. We

obtained the transverse sound velocity V_T and longitudinal sound velocity V_L by using the following equations.

$$V_T = \sqrt{\frac{G}{\rho}}, V_L = \sqrt{\frac{K + \frac{4}{3}G}{\rho}} \tag{3.2}$$

where ρ is density. The calculated V_L, V_T, and ρ values for those minerals are listed in Table 4. Both V_L and V_T were greater in muscovite than the other two. These values could be useful in the geosciences area and used for seismology databases.

Table 4: Values of density and sound velocities V_L and V_T.

Crystal	ρ (g/cm^3)	V_L(m/s)	V_T(m/s)
Kaolinite	2.58	5885	3512
Muscovite	2.71	6208	3756
MMT	2.76	4797	2933

3.4 Conclusion

We presented detailed results on the first-principles calculation of the electronic structure, interatomic bonding, partial charge, optical properties, and mechanical properties. The three crystals had wide band gaps, showing their insulating nature. The O-H bonds were the strongest bond, with the largest BO of around 0.29 e in the three crystals. In addition, Si-O bonds were

reasonably strong and had the highest percentage contribution of the three crystals. Based on TBOD, kaolinite was slightly more cohesive than MMT or muscovite. Muscovite had the highest plasmon frequency of 23.59 eV. Despite similar compositions specifically in kaolinite and MMT, we obtained somewhat different results for their mechanical properties. Muscovite had a higher bulk, shear, Young's modulus, and Vicker's hardness. As a result of the higher Pugh's modulus ratio, MMT was more brittle than kaolinite or muscovite. The presented work is the first step in understanding the structure and properties of these three clay minerals. We plan to extend this study to include the influence of dopant Mg and Na.

CHAPTER 4

ELECTRONIC STRUCTURE AND MECHANICAL PROPERTIES OF SOLVATED MONTMORILLONITE CLAY USING LARGE-SCALE DFT METHOD

4.1 Introduction

In recent years, ab initio approaches have grown increasingly prominent in material research. They have led to a number of impressive discoveries [93, 62] and successful applications of DFT to study the electronic structure and properties of atoms, molecules, and solids. For example, DFT calculations have been used to predict the stability and reactivity of transition metal catalysts, which are widely used in chemical reactions.

MMT clay is a type of smectite clay mineral. It is naturally abundant and can be chemically modified through the cation exchange [47, 50, 21]. Weathering of eruptive rock materials leads to the formation of MMT. MMT is considered to be a valuable model for studying the properties of smectite clay minerals, owing to its high swelling capacity and ability to produce stable suspensions [48]. Crystalline MMT has a layered structure that is characteristic of smectites, consisting of two tetrahedral sheets sandwiching a central octahedral sheet, as shown in Figure 8. Its layer charge and ex-

changeable cations are easily modifiable, making it a versatile material for investigating the properties of smectite clay minerals. Moreover, crystalline MMT has been widely studied in the literature, and its properties and behaviors are well documented, making it an excellent reference material for exploring other smectites. MMT is a class of materials that is hydrophilic and is capable of absorbing cations [2]. Therefore, it can be used in numerous fields, such as oil refining, pharmaceutical preparations, sugar refining, catalyst, and as a binder for insulating materials [27]. Moreover, MMT is used to design polymer-clay nanocomposites, which are capable of changing its strength and resistance . Furthermore, it can form composites of biological entities, such as proteins and amino acids [35]. Computational modelling can provide valuable information to gain insight into the complex structures of clay minerals, including solvated montmorillonite (MMT). In comparison to crystalline MMT, the solvated MMT is far more challenging to study due to the presence of water [31, 80] and other elements, such as Na, Mg, and Cl between these layers. Na^{+}has been identified as the main electric charge carrier [78] of the MMT layer. When a divalent metal ion takes the place of an aluminum ion in octahedral structure of MMT, it results in having a net negative charge. This layer attracts or binds to positively charged ions (also known as exchangeable cations), such as sodium, potassium, calcium, and magnesium, leading to the formation of an interlayer hydrated phase.

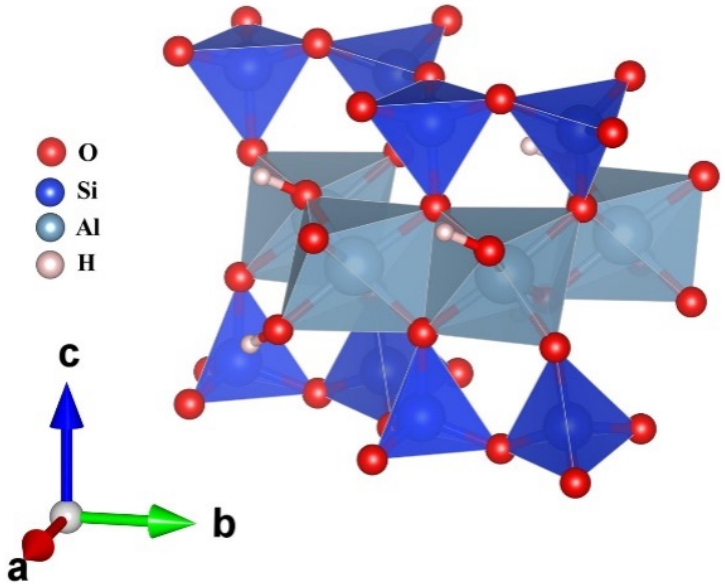

Figure 8: Polyhedral structure for crystalline MMT model. $SiO_4 tetrahedra and AlO_6 octahedra are shown in blue and light blue, respectively.$

These changes to the structure may have environmental impacts since they affect the mineral's ability to adsorb and release ions and molecules, which can influence soil fertility, nutrient cycling, and water retention.

Understanding and predicting MMT clay's interactions with water and other environmental fluids is a critical topic in geotechnical engineering, geo-environmental engineering, industrial applications, such as muds for oil well drilling, and water treatment. MMT clay possesses a remarkable capacity to absorb water into its interlayer spaces. This water absorption triggers a reaction within the clay, leading to its swelling. Due to the significant interest in understanding and predicting the swelling behavior of MMT clay,

it becomes essential to develop and study a precise model that can effectively explain and forecast this phenomenon.

To gain a deeper understanding of various material properties, researchers can employ a range of approaches, such as theoretical simulations and experimental studies. These methods can establish meaningful correlations and comparisons between different properties, providing valuable insights and a wider perspective. Nevertheless, performing experimental research can be an expensive undertaking in terms of time and money due to the requirement for multiple physical fabrication attempts and practical limitations while computational simulations, such as the orthogonalized linear combination of atomic orbitals (OLCAO) [10] and molecular dynamic (MD), supported by robust algorithms and valid theoretical models, have emerged as a crucial element in contemporary research. These simulations serve as a bridge between theory and experiments [20]. OLCAO is a powerful computational tool for studying the electronic structure and properties of materials. This method can calculate complex systems with up to mote than 4000 atoms, making it useful for investigating a wide range of materials, including complex minerals and alloys. By combining these approaches, researchers can gain a comprehensive understanding of the relationships between different material properties, paving the way for new discoveries and applications in materials science.

In this work, we performed detailed DFT calculations on the solvated

MMT model. The model consists of 4071 atoms with metallic elements, such as Na, Mg and Cl. Details of the solvated model are described in Section 2. We focus on the electronic structure, interatomic bonding, mechanical properties, and partial charge distributions of the solvated MMT. The electronic structure and properties of materials have been altered by the presence of both metallic elements and water molecules, leading to the possibility of unexpected applications. From the interatomic bonding, we have provided critical parameters, such as total and partial bond order density (TBOD and PBOD). The bond order can provide information about the internal cohesion of a material. Additionally, these parameters can be utilized to compare dissimilar materials and identify similarities and differences in their bonding behavior, thereby facilitating the design and optimization of materials with specific properties and functions.

4.2 Model Construction

The original model, created by N. Subramanian et al. [71] was constructed with five layers of MMT clay stacked on top of each other. This unit cell is then replicated in the $\mathrm{a} - \mathrm{b}$ plane, followed by isomorphic substitution of Mg^{2+} for Al^{3+} in the octahedral sheet to produce a MMT layer with hydroxyl groups in places compatible with experimental results for Wyoming-MMT with a charge of $-0.57\mathrm{e}^{-}$ per unit cell $\left(\mathrm{O}_{20}(\mathrm{OH})_4[9].\mathrm{Na}^{+}\right.$ was added to

neutralize the net structural charge of the MMT layer. N. Subramanian et al., created the molecular structure of MMT using HRTEM lattice parameters as a monoclinic unit cell in the $C121$ space group; the lattice constants $a = 5.25\mathring{A}, b = 9.03\mathring{A}, c = 10.07\mathring{A}$, and $\beta = 99.5^{\circ}$ from Douillard et al. [17]. The solvated MMT layer used in this work was extracted from the model of N. Subramanian et al, as illustrated in Figure 9. The solvated MMT model of N. Subramanian et al. mainly has one layer, that is replicated five times to form a large model. We chose to extract only one layer since we have a periodic boundary condition in our model. One of the major difficulties we encountered during the extraction for the solvated MMT layer was the cell size, which needs to be optimized. This has been successfully resolved by optimization via VASP code [39, 38]. The optimized lattice parameters are a = $51.29\mathring{A}$, b = $49.12\mathring{A}$, and c = $18.27\mathring{A}$. The final large supercell model has 4071 atoms including 1057 water molecules.

4.3 Computation Methods

The VASP package is employed to thoroughly optimize the structure of large solvated MMT model (see section 2.2). We used an energy cut-off of 600eV, with electronic force convergence at $10 - 5$eV, and single KPOINTS for the large solvated MMT model. The optimized structure obtained from VASP is used as input in the OLCAO calculation for electronic structure

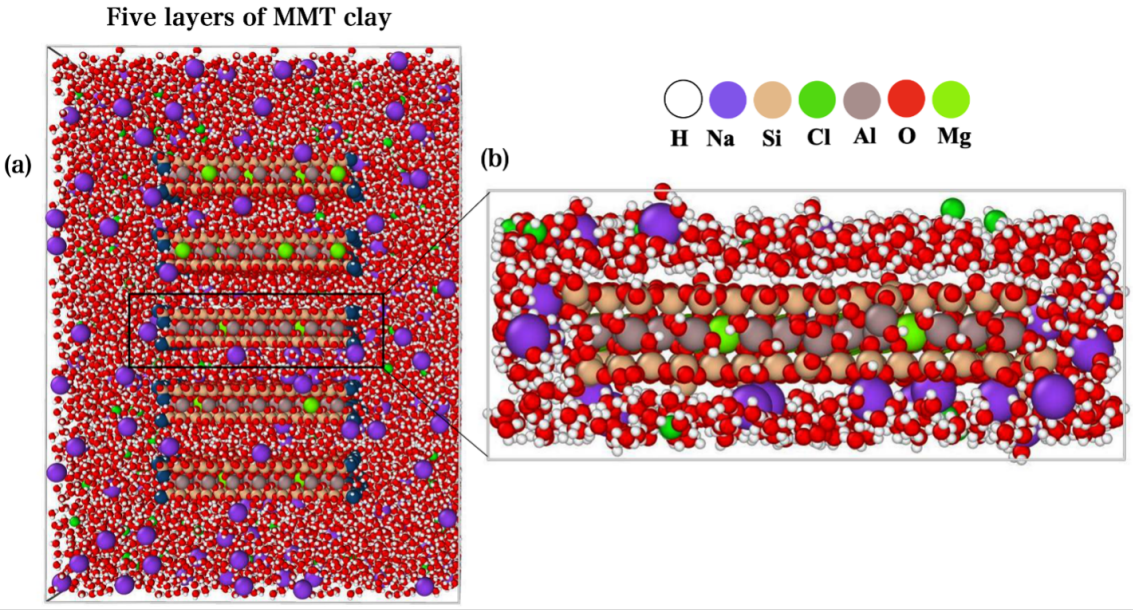

Figure 9: Two-dimensional (2D) structure sketch of (a) N. Subramanian et al. model with five layers of MMT. The (b) extracted layer for solvated MMT model in ball and stick form.

and interatomic bonding. OLCAO method uses atomic orbitals in the basis expansion [11]. The combination of OLCAO method with VASP has been very successful in electronic property calculations, especially for large and complex systems. This success is due to the flexibility and economic use of the basis set [12, 1, 37].

4.4 Results and Discussion

4.4.1 Electronic Structure and interatomic Bonding

Total density of states (TDOS) and atom-resolved partial DOS (PDOS) are the most effective ways to summarize the electronic structures of a material. In this investigation, the DOS computation was carried out using minimal basis (MB). These results for solvated MMT are compared with crystalline MMT [73] and shown in Figure 10. We also calculated the TDOS and PDOS for both models within an energy range from -20.21eV to 15.88eV. In the crystalline MMT, the valance band (VB) DOS has the highest peak at -1.5eV, while the highest peak in solvated MMT is at -8.5eV. In crystalline MMT, the DOS in the conduction band (CB) has multiple peaks ranging from 6eV to 15.88eV, which mostly originates from O, Si, and Al atoms. Whereas in solvated MMT, there is a single prominent peak at 8.5eV, which originates from O. The atom-resolved PDOS summarizes the contributions from each atom to the VB and CB. In both cases, it shows the lower part of the VB DOS mainly originating from the O atoms. There is a clear HOMO-LUMO band gap (E_{gap}) of 5.11eV in the crystalline model, but no band gap in the solvated model due to the presence of water molecules. Both oxygen and hydrogen atoms are filling the gap with further interaction to Si and Al atoms. It is important to note that the location of 0eV is not the same. The 0eV is

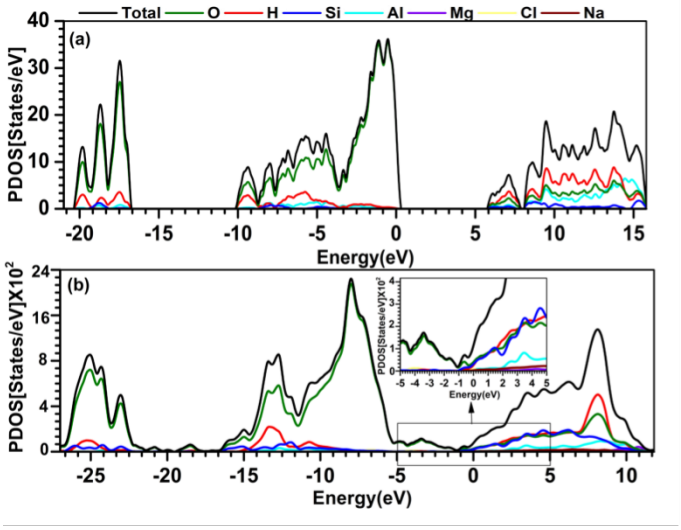

Figure 10: Calculated TDOS and PDOS of the (a) crystalline MMT model, (b) solvated MMT model with inset focused on -5 eV to 5 eV. The atom-resolved PDOS is shown in color. O: green; H: red; with inset focused on −5 eV to 5 eV. The atom-resolved PDOS is shown in color. O: green; H: red; Si: blue; Al: light blue; Mg: purple; Cl: yellow; Na: brown.

at the highest occupied state at HOMO-LUMO. In the solvated model, the water molecules occupied those states. Furthermore, solvation refers to the process of dissolving a material in a solvent, which can result in the formation of a solvated shell around the material. The solvation shell can interact with MMT's electronic orbital, leading to changes in their energy levels or charge distribution. As a result, we can claim that when the size of the alkali ions increases, the band gap decreases as in the hydrated MMT.

The most critical component of the electronic structure is interatomic

bonding. Crystalline MMT has only four types of bonds: $O-H, Si-O, Al-O$, and $O\cdots H$, which are also in the solvated model. The solvated MMT is significantly more complicated. It has a total of fifteen types of bonds: $Al-H, Al-O, Cl-H, Cl-Na, Cl-O, H-H, H-Mg, H-Na, O-H, O\cdots H$, $H-Si, Mg-O, Na-O, O-O$, and $Si-O$. In crystalline MMT, the $O-H$ bond exhibits a strong bond with a bond order (BO) value of approximately $0.29e^{-}$, as depicted in Figure 11a. Additionally, there are some hydrogen bonds (HB) $O\cdots H$ with very low BO and larger bond length (BL) between 2.47 and $3.49\mathring{A}$. The Si-O and higher BO are followed by Al-O bonds and both bonds act as a unit in the crystalline MMT. In solvated MMT, there is a wide range of BO for $O-H, Si-O$, and $Al-O$ bonds. It is worth noting that the bond length has lower variation, while the bond order fluctuates significantly. This fluctuation in bond order could be explained by the presence of water molecules. Additionally, there is a notable presence of weak $O\cdots H$ bonds ranging from $1.50\mathring{A}$ to $3.49\mathring{A}$. In solvated MMT, O-O bond has the strongest BO value of around $0.51e^{-}$, followed by the $H-H$ bond with a BO value of approximately $0.47e^{-}$, as shown in Figure 11b . Interestingly, there are short $H-H$ bonds with higher BO in the solvated MMT. These short $H-H$ bonds are from two different H_2O molecules. $Mg-O$ and $Na-O$ have bonds with noticeable BO. $Cl-H$ has higher BO of around $0.28e^{-}$in comparison to $Al-H, H-Mg, H-Na$, and $H-Si$ bonds. $Al-H, H-Mg, H-Si$,

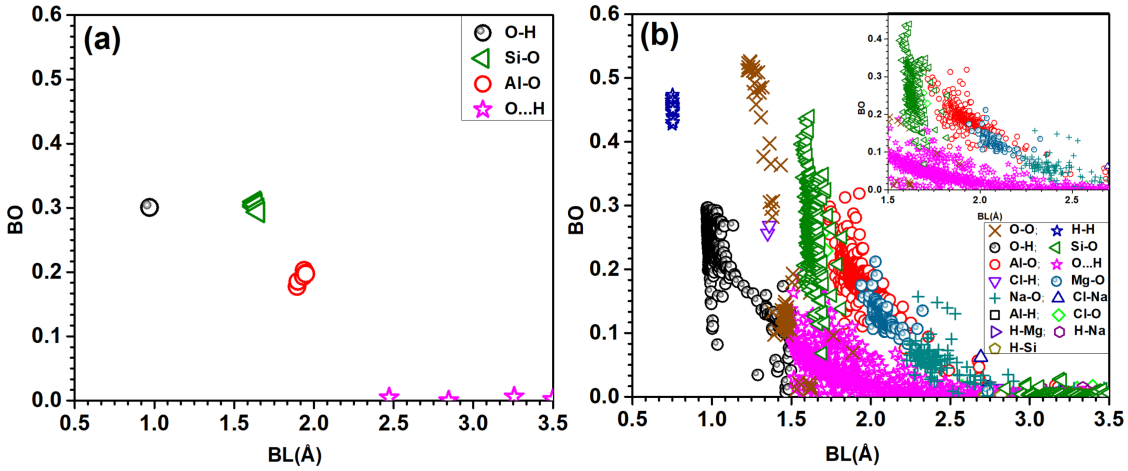

Figure 11: (a) BO vs. BL distributions for all atomic pairs in the (a) crystalline MMT model and (b) solvated MMT with inset focused on BL from 1.5 Å to 2.7 Å.

and $H-Na$ have lower BO at higher BL and are overlapped by other data in Figure 11b. There is one $Cl-Na$ bond with BO of $0.06e^{-}$at $2.69\mathring{A}$. These bonds may not have a strong effect in the solvated MMT.

TBOD is a useful metric to study the crystal cohesiveness. The TBOD for the crystalline MMT is $0.033e^{-}/\mathring{A}^3$, whereas for the solvated MMT, it is $0.022e^{-}/\mathring{A}^3$. To identify the reason behind lower TBOD in solvated MMT, we further analyzed the percentage contribution from the PBOD for each type of bond as shown in Figure 12. Si-O bonds with 62.29% contribution in TBOD of crystalline MMT is significantly higher. Si-O bonds form a strong three-dimensional network of tetrahedral sheets, providing structural stability and cohesiveness. On the other hand, solvated MMT contains

water molecules and exchangeable cations between the layers, which create weaker electrostatic interactions with the mineral, reducing its overall cohesiveness. Although the Si-O bonds in solvated MMT are also covalent in nature, they contribute less to the stability than in crystalline MMT. Therefore, understanding the difference in the contribution of $Si-O$ bonds between the two types of MMT is essential for understanding their distinct physical and chemical properties. We observe that the Al-O bonds also make higher contribution of 29.67% in crystalline MMT in comparison to solvated MMT with modest contribution of 12.34%. The presence of water in solvated MMT leads to the formation of a strong hydrogen [95] bonding network between the absorbed water in the interlayer, which is energetically favorable and exothermic. These findings have significant implications for applications, such as nuclear waste storage. In addition, the strong $O-H$ bonds found in water molecules as well as in the hydroxyl groups have key contribution of 44.17% in the solvated MMT. Whereas the $O-H$ bonds have only 7.72% contribution in crystalline MMT. Following a similar pattern, the solvated MMT has higher $O\cdots H$ contribution in comparison to crystalline MMT. Higher $O-H$ and O.H contribution in the solvated MMT is clearly due to water molecules, since MMT is known to be hydrophilic and this notable characteristic differentiates it from crystalline MMT and other clay minerals. Furthermore, there is a very low contribution of $Mg-O, O-O$,

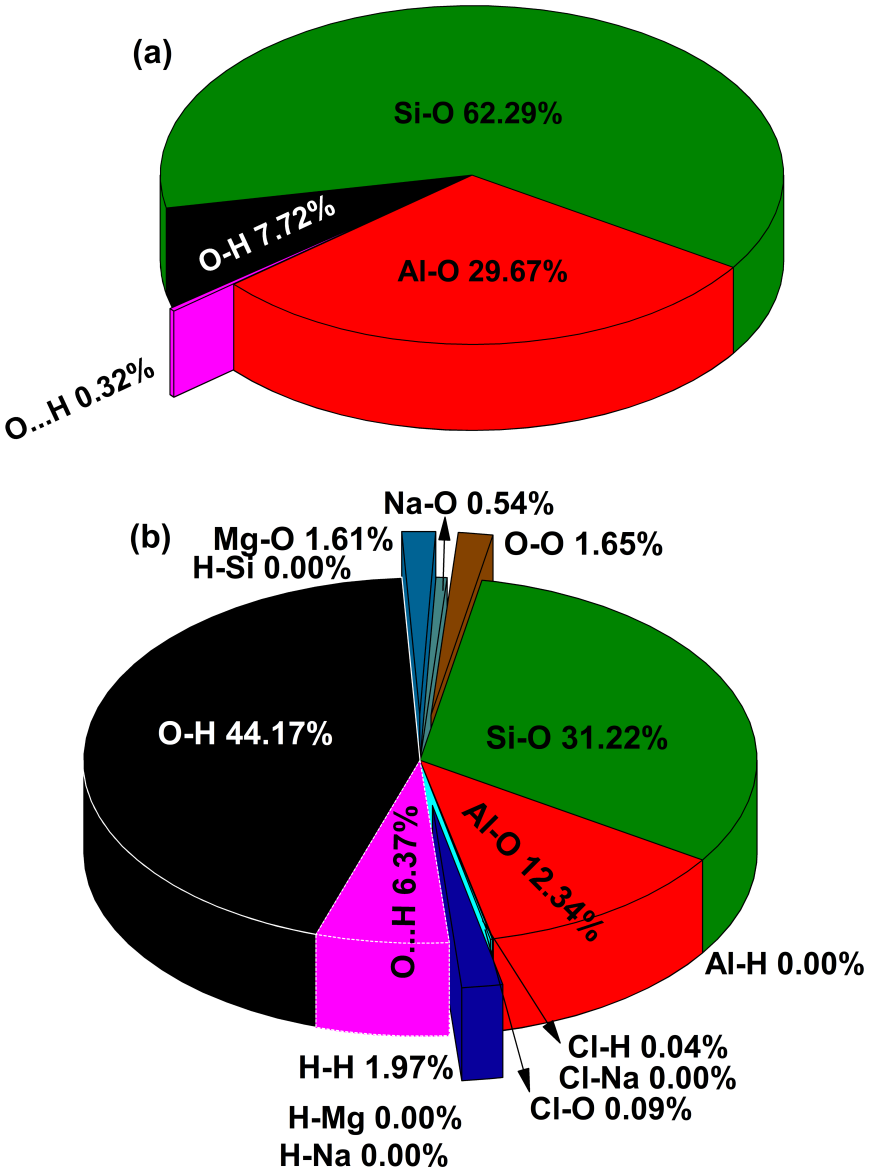

Figure 12: Pie chart for the pair contributions of (a) Crystalline MMT model and (b) solvated MMT model.

and $H - H$ bonds as shown in Figure 12 b. The lower BO contribution of $Al - H, Cl - Na, H - Na, H - Mg$, and $H - Si$ bonds leads to negligible percentage contribution in TBOD. Solvated MMT leads to a significantly more complicated bonding arrangement and a wide range of BO values. A comprehensive explanation of interatomic bonding in a complex system, as this large model shows, is a challenging endeavor.

4.4.2 Mechanical Properties

The study of mechanical properties of clay minerals is critical, particularly for engineering[68, 52]. However, due to their tiny particle size the mechanical properties of clay minerals are difficult to evaluate directly. It is hard to isolate a large enough individual crystal of clay and impossible to directly measure their acoustic properties. However, we employed a computational approach using VASP to calculate the elastic coefficients for both crystalline and solvated MMT. Table 5 shows the calculated mechanical properties of crystalline and solvated MMT. The calculated mechanical properties are bulk modulus (k = G/K), and Vicker's hardness (H_v). Shear modulus (G) measures how resistant a material is to shear deformation. On the other hand, bulk modulus (K) measures a material's resistance to volume compression. The compressibility of a material increases as its K decreases. Additionally, the sound velocity is closely related to the G and K, making it a useful pa-

rameter for analyzing the seismic and sonic log data [51]. Finally, Young's modulus (E) measures how stiff a material is or how well it can resist deforming in the direction of an applied force. This study compares the mechanical properties of the solvated model to the crystalline model and reveals a significant decrease in the G, K, and E of solvated MMT. This implies that water solvation in MMT reduces the mechanical strength. However, the Poisson's ratio of both models remains similar, exhibiting only slight variations in their values. This means that water has no effect on the material's ability to contract laterally while being stretched longitudinally. It is also interesting to note that Pugh's modulus ratio and Vicker's hardness are slightly lower for solvated MMT. This indicates that solvated MMT is less stiff and less resistant to deformation than crystalline MMT. We were unable to find any experimental data on the mechanical properties of solvated MMT for compositions analogous to those used in this study. In order to visualize the anisotropy of the Young's and shear moduli, we have plotted the three-dimensional (3D) anisotropic surface figures using ELATE [22] software for both crystalline and solvated MMT in Figure 13. The surfaces of Young's modulus are shown in green color in both crystalline and solvated MMT, indicating the positive values. The degree of deviation of the surfaces in Young's and shear moduli from the spherical shape determines the anisotropy. Figure 13a, b shows that the degree of elastic anisotropy in Young's and shear moduli is higher

in crystalline MMT compared to solvated MMT, as shown in Figure 13c,d. This can be attributed to the fact that crystalline MMT has a more spherical shape in all three planes, which leads to a more isotropic distribution [96]. In solvated MMT, the presence of absorbed water molecules in the interlayer region causes the clay to swell, resulting in a more elongated shape and a higher degree of elastic anisotropy. In contrast, crystalline MMT has a more compact and ordered structure, which leads to a lower degree of anisotropy in its elastic properties.

Table 5: The calculated bulk modulus (K), shear modulus (G), Young's modulus (E), Poisson's ratio (η), Pugh's modulus ratio (k = G/K), and Vicker's hardness (H_V) for crystalline and solvated models.

Model	K (GPa)	G (GPa)	E (GPa)	η	G/K	$H_V(GPa)$
Cryst-MMT*	31.85	23.74	57.05	0.2015	0.7453	6.201
Solv-MMT	21.55	16.03	38.53	0.2019	0.7438	4.685

* From reference [73].

It is crucial to determine the sound velocities once we have the elastic tensors for the solvated MMT. In Table 6 , we compare the calculated densities, V_L and V_T, of crystalline and solvated MMT. In the solvated MMT, V_L and V_T are both larger than in the crystalline case. These results may have applications in seismology and geosciences. The values of V_L and V_T can be used to determine the elastic properties of a material and to infer its geological structure. Compared with other clay minerals, such as illite,

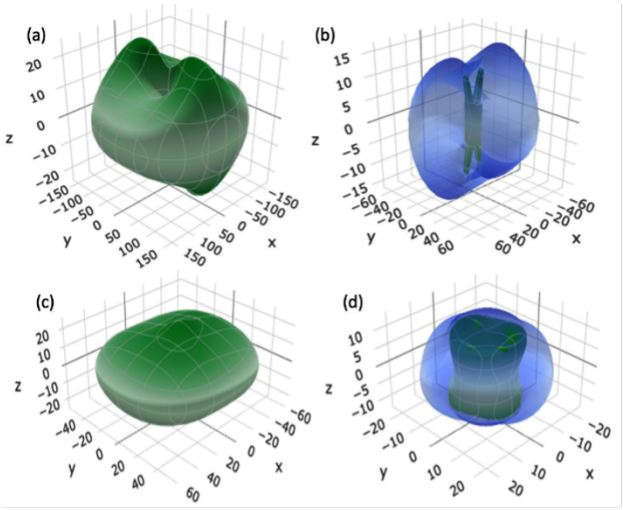

Figure 13: A 3D representation of (a) Young's modulus and (b) shear modulus for crystalline MMT; (c) Young's modulus and (d) shear modulus for solvated MMT model.

it has been found that the elastic properties of MMT are highly dependent on the layer charge density and the nature of the interlayer cations. This makes them a potentially useful tool for exploring geological structures and characterizing subsurface environments.

In particular, the high swelling capacity of MMT and its ability to form stable suspensions make it a promising candidate for use in drilling fluids, where it can help in stabilizing boreholes and prevent blowouts.

Table 6: Density (ρ) and values of sound velocities (V_L and V_T).

Model	$\rho\,(g/cm^3)$	$V_L(m/s)$	$V_T(m/s)$
Cryst-MMT*	2.76	4797	2933
Solv-MMT	1.64	5115	3126

*From reference [73].

4.5 Conclusion

In this work, we explore the computational simulation of montmorillonite (MMT) in both crystalline and solvated forms. Our study presents a comprehensive analysis of the electronic structure, interatomic bonding, and mechanical properties for solvated MMT clay mineral. This is the first study on solvated MMT using large-scale supercell modelling based on density functional theory (DFI). Our meticulous analysis involves bonds between each pair of atoms in the solvated MMT model, which reveals the complexity of covalent and hydrogen bonds. One of the key findings is that the presence of water in this model leads to a strong hydrogen bonding network with adsorbed water molecules in the interlayer. The $O-H, Si-O, Al-O$, and O.H are important components of interatomic bonding, which is found in both crystalline and solvated MMT. We can see that $O-H$ and $O\cdots H$ bonds have a higher contribution in the solvated MMT compared to crystalline MMT due to water molecules. Conversely, the $Si-O$ and $Al-O$ bonds have less contribution in the solvated MMT compared to crystalline MMT. Moreover, our analysis of the electronic structure revealed a single prominent peak in the DOS in the conduction band (CB) located at -8.5eV in the solvated MMT model. In addition, we analyzed the atom-resolved partial density of states (PDOS) to determine the contributions made by each atom in the VB and CB. We found that the majority of the lower part of the VB DOS origi-

nates from the O atom, while the CBDOS is contributed by H atoms. One of the most significant findings is that the solvation of montmorillonite (MMT) leads to a significant decrease in its mechanical strength, as evidenced by reduced values of G, K, and E. The presence of water does not affect the material's lateral contraction ability while being longitudinally stretched, as indicated by similar Poisson's ratios for solvated and crystalline MMT. These results from mechanical properties also reveal important insights into sound velocities. Comparing the densities, V_L and V_T, we observe that both values of V_L and V_T are higher in solvated MMT compared to crystalline MMT, while the converse is true in densities. Our findings have implications for the potential application of MMT clay in environmental applications as a landfill barrier and toxic waste repository. In summary, our study sheds light on the electronic structure and bonding network of solvated MMT clay, which can guide future research into its potential applications.

CHAPTER 5

FINAL REMARKS AND FUTURE WORK

There are numerous opportunities to advance the study of clay minerals, especially for Montmorillonite (MMT) clay. In the following, we outline potential avenues for further exploration:

1- Enhance solvation models within VASP to better capture interactions between Montmorillonite clay and solvent molecules. we will consider utilizing advanced solvation techniques like the embedded cluster method or explicit solvent models available in VASP.

2- Thinking of exploring the use of hybrid functionals within VASP to enhance the accuracy of electronic structure predictions. Hybrid functionals, combining the strengths of Hartree-Fock and DFT, offer a more precise description of electronic interactions.

3- Implement machine learning techniques to predict electronic and mechanical properties based on results obtained from VASP and OLCAO simulations. This approach can significantly expedite property evaluations and facilitate high-throughput screening.

4- Improve accuracy in intermolecular interactions by incorporating advanced dispersion corrections within VASP. This becomes particularly crucial when studying solvated systems where dispersion forces play a pivotal role.

5- Collaboration with Experimentalists: Foster close collaboration with experimental researchers to design experiments that complement and validate computational findings. This collaborative approach enhances the applicability and reliability of the results by combining insights from both computational and experimental perspectives.

These future work suggestions aim to refine and extend the understanding of electronic structure and mechanical properties of solvated Montmorillonite clay, leveraging the capabilities of VASP and OLCAO.

APPENDIX A

Input files INCAR, KPOINTS and POSCAR used for VASP calculation are listed.

INCAR file for Kaolinite.

System = $Si_2Al_2O_9H_4$

ISMEAR = -5 ! Use 0 for KPOINTS less than 4 otherwise -5.

PREC = Accurate ! low, medium, normal are other options. Use suitable one.

ENCUT = 600 eV ! Decide considering the crystal size and accuracy you want.

EDIFF = 1.0E-5 ! Enegy difference covergence limit for electronic optimization.

EDIFFG = -1.0E-3 ! Enegy difference covergence limit for ionic optimization.

IBRION = 1 ! 0 for MD, 1 best, 2 for diff relaxation problems. Othere numbers for diffrent cases.

NSW = 3000 ! Total number of ionic steps.

ISIF = 3 ! 2 and 4 ionic, 7 volume and 3 both.

LREAL = Auto ! Projection on real space. use FALSE (default) for reciprocal space.

NPAR = 12 ! Best sqrt of NCPUs used. should be ¿= NCPUs/32.

ALGO = Fast ! default is Normal.

LCHARG = F ! No writting in CHG and CHGCAR files

LWAVE = F

INCAR file for Muscovite.

System = $Al_{24}O_{96}Si_{24}K_8H_{16}$

ISMEAR = 0 ! Use 0 for KPOINTS less than 4 otherwise -5.

PREC = Accurate ! low, medium, normal are other options. Use suitable one.

ENCUT = 600 eV ! Decide considering the crystal size and accuracy you want.

EDIFF = 1.0E-5 ! Enegy difference covergence limit for electronic optimization.

EDIFFG = -1.0E-3 ! Enegy difference covergence limit for ionic optimization.

IBRION = 1 ! 0 for MD, 1 best, 2 for diff relaxation problems. Othere numbers for diffrent cases.

NSW = 3000 ! Total number of ionic steps.

ISIF = 3 ! 2 and 4 ionic, 7 volume and 3 both.

LREAL = Auto ! Projection on real space. use FALSE (default) for reciprocal space.

NPAR = 12 ! Best sqrt of NCPUs used. should be ¿= NCPUs/32.

ALGO = Fast ! default is Normal.

LCHARG = F ! No writting in CHG and CHGCAR files

LWAVE = F ! No writting in WAVECAR file

INCAR file for Montmorillonite.

System = $Al_4Si_8O_{24}H_4$

ISMEAR = 0 ! Use 0 for KPOINTS less than 4 otherwise -5.

PREC = Accurate ! low, medium, normal are other options. Use suitable one.

ENCUT = 600 eV ! Decide considering the crystal size and accuracy you want.

EDIFF = 1.0E-5 ! Enegy difference covergence limit for electronic optimization.

EDIFFG = -1.0E-3 ! Enegy difference covergence limit for ionic optimization.

IBRION = 1 ! 0 for MD, 1 best, 2 for diff relaxation problems. Othere numbers for diffrent cases.

NSW = 3000 ! Total number of ionic steps.

ISIF = 3 ! 2 and 4 ionic, 7 volume and 3 both.

LREAL = Auto ! Projection on real space. use FALSE (default) for reciprocal space.

NPAR = 12 ! Best sqrt of NCPUs used. should be ¿= NCPUs/32.

ALGO = Fast ! default is Normal.

LCHARG = F ! No writting in CHG and CHGCAR files

LWAVE = F ! No writting in WAVECAR file

KPOINT file used for Kaolinite.

0

G

6 6 4

0 0 0

KPOINT file used for Muscovite.

G

0

G

2 2 1

0 0 0

KPOINT file used for Montmorillonite.

G

0

G

2 1 1

0 0 0

POSCAR file used for Kaolinite.

System $Si_2Al_2O_9H_4$

1.00

5.15500000 0.00000000 0.00000000

2.56346200 4.47243600 0.00000000

0.75860800 1.75409000 7.15413900

Si Al O H

2 2 9 4

Direct

0.631600000000 0.638600000000 0.090900000000

0.314600000000 0.292800000000 0.091300000000

0.666700000000 0.783700000000 0.472100000000

0.326700000000 0.453300000000 0.469900000000

0.606000000000 0.568300000000 0.317000000000

0.373900000000 0.181100000000 0.317500000000

0.505400000000 0.000000000000 0.000000000000

0.973200000000 0.450100000000 0.024700000000

0.442800000000 0.530000000000 0.003200000000

0.996100000000 0.797900000000 0.322000000000

0.620600000000 0.066800000000 0.605100000000

0.382600000000 0.686300000000 0.608000000000

0.004800000000 0.445900000000 0.609400000000

0.729100000000 0.022400000000 0.723200000000

0.011200000000 0.297500000000 0.728600000000

0.284200000000 0.744300000000 0.725800000000

0.998000000000 0.985900000000 0.329500000000

POSCAR file used for Muscovite.

System $Al_{24}O_{96}Si_{24}K_8H_{16}$

1.00

10.37800000 0.00000000 0.00000000

0.00000000 8.99600000 0.00000000

-1.81436600 0.00000000 20.01392700

Al O Si K H

24 96 24 8 16

Direct

0.124200000000 0.087100000000 0.001600000000

0.624200000000 0.087100000000 0.001600000000

0.375800000000 0.087100000000 0.498400000000

0.875800000000 0.087100000000 0.498400000000

0.375800000000 0.912900000000 0.998400000000

0.875800000000 0.912900000000 0.998400000000

0.124200000000 0.912900000000 0.501600000000

0.624200000000 0.912900000000 0.501600000000

0.374200000000 0.587100000000 0.001600000000

0.874200000000 0.587100000000 0.001600000000

0.125800000000 0.587100000000 0.498400000000

0.625800000000 0.587100000000 0.498400000000

0.125800000000 0.412900000000 0.998400000000

0.625800000000 0.412900000000 0.998400000000

0.374200000000 0.412900000000 0.501600000000

0.874200000000 0.412900000000 0.501600000000

0.731250000000 0.924200000000 0.137200000000

0.768750000000 0.924200000000 0.362800000000

0.768750000000 0.075800000000 0.862800000000

0.731250000000 0.075800000000 0.637200000000

0.981250000000 0.424200000000 0.137200000000

0.518750000000 0.424200000000 0.362800000000

0.518750000000 0.575800000000 0.862800000000

0.981250000000 0.575800000000 0.637200000000

0.232500000000 0.945000000000 0.052700000000

0.732500000000 0.945000000000 0.052700000000

0.267500000000 0.945000000000 0.447300000000

0.767500000000 0.945000000000 0.447300000000

0.267500000000 0.055000000000 0.947300000000

0.767500000000 0.055000000000 0.947300000000

0.232500000000 0.055000000000 0.552700000000

0.732500000000 0.055000000000 0.552700000000

0.482500000000 0.445000000000 0.052700000000

0.982500000000 0.445000000000 0.052700000000

0.017500000000 0.445000000000 0.447300000000

0.517500000000 0.445000000000 0.447300000000

0.017500000000 0.555000000000 0.947300000000

0.517500000000 0.555000000000 0.947300000000

0.482500000000 0.555000000000 0.552700000000

0.982500000000 0.555000000000 0.552700000000

0.212500000000 0.260000000000 0.054200000000

0.712500000000 0.260000000000 0.054200000000

0.287500000000 0.260000000000 0.445800000000

0.787500000000 0.260000000000 0.445800000000

0.287500000000 0.740000000000 0.945800000000

0.787500000000 0.740000000000 0.945800000000

0.212500000000 0.740000000000 0.554200000000

0.712500000000 0.740000000000 0.554200000000

0.462500000000 0.760000000000 0.054200000000

0.962500000000 0.760000000000 0.054200000000

0.037500000000 0.760000000000 0.445800000000

0.537500000000 0.760000000000 0.445800000000

0.037500000000 0.240000000000 0.945800000000

0.537500000000 0.240000000000 0.945800000000

0.462500000000 0.240000000000 0.554200000000

0.962500000000 0.240000000000 0.554200000000

0.226500000000 0.558000000000 0.052000000000

0.726500000000 0.558000000000 0.052000000000

0.273500000000 0.558000000000 0.448000000000

0.773500000000 0.558000000000 0.448000000000

0.273500000000 0.442000000000 0.948000000000

0.773500000000 0.442000000000 0.948000000000

0.226500000000 0.442000000000 0.552000000000

0.726500000000 0.442000000000 0.552000000000

0.476500000000 0.058000000000 0.052000000000

0.976500000000 0.058000000000 0.052000000000

0.023500000000 0.058000000000 0.448000000000

0.523500000000 0.058000000000 0.448000000000

0.023500000000 0.942000000000 0.948000000000

0.523500000000 0.942000000000 0.948000000000

0.476500000000 0.942000000000 0.552000000000

0.976500000000 0.942000000000 0.552000000000

0.204000000000 0.096000000000 0.168000000000

0.704000000000 0.096000000000 0.168000000000

0.296000000000 0.096000000000 0.332000000000

0.796000000000 0.096000000000 0.332000000000

0.296000000000 0.904000000000 0.832000000000

0.796000000000 0.904000000000 0.832000000000

0.204000000000 0.904000000000 0.668000000000

0.704000000000 0.904000000000 0.668000000000

0.454000000000 0.596000000000 0.168000000000

0.954000000000 0.596000000000 0.168000000000

0.046000000000 0.596000000000 0.332000000000

0.546000000000 0.596000000000 0.332000000000

0.046000000000 0.404000000000 0.832000000000

0.546000000000 0.404000000000 0.832000000000

0.454000000000 0.404000000000 0.668000000000

0.954000000000 0.404000000000 0.668000000000

0.122500000000 0.802000000000 0.162000000000

0.622500000000 0.802000000000 0.162000000000

0.377500000000 0.802000000000 0.338000000000

0.877500000000 0.802000000000 0.338000000000

0.377500000000 0.198000000000 0.838000000000

0.877500000000 0.198000000000 0.838000000000

0.122500000000 0.198000000000 0.662000000000

0.622500000000 0.198000000000 0.662000000000

0.372500000000 0.302000000000 0.162000000000

0.872500000000 0.302000000000 0.162000000000

0.127500000000 0.302000000000 0.338000000000

0.627500000000 0.302000000000 0.338000000000

0.127500000000 0.698000000000 0.838000000000

0.627500000000 0.698000000000 0.838000000000

0.372500000000 0.698000000000 0.662000000000

0.872500000000 0.698000000000 0.662000000000

0.131450000000 0.371300000000 0.167400000000

0.631450000000 0.371300000000 0.167400000000

0.368550000000 0.371300000000 0.332600000000

0.868550000000 0.371300000000 0.332600000000

0.368550000000 0.628700000000 0.832600000000

0.868550000000 0.628700000000 0.832600000000

0.131450000000 0.628700000000 0.667400000000

0.631450000000 0.628700000000 0.667400000000

0.381450000000 0.871300000000 0.167400000000

0.881450000000 0.871300000000 0.167400000000

0.118550000000 0.871300000000 0.332600000000

0.618550000000 0.871300000000 0.332600000000

0.118550000000 0.128700000000 0.832600000000

0.618550000000 0.128700000000 0.832600000000

0.381450000000 0.128700000000 0.667400000000

0.881450000000 0.128700000000 0.667400000000

0.231250000000 0.924200000000 0.137200000000

0.268750000000 0.924200000000 0.362800000000

0.268750000000 0.075800000000 0.862800000000

0.231250000000 0.075800000000 0.637200000000

0.481250000000 0.424200000000 0.137200000000

0.018750000000 0.424200000000 0.362800000000

0.018750000000 0.575800000000 0.862800000000

0.481250000000 0.575800000000 0.637200000000

0.229650000000 0.255000000000 0.136500000000

0.729650000000 0.255000000000 0.136500000000

0.270350000000 0.255000000000 0.363500000000

0.770350000000 0.255000000000 0.363500000000

0.270350000000 0.745000000000 0.863500000000

0.770350000000 0.745000000000 0.863500000000

0.229650000000 0.745000000000 0.636500000000

0.729650000000 0.745000000000 0.636500000000

0.479650000000 0.755000000000 0.136500000000

0.979650000000 0.755000000000 0.136500000000

0.020350000000 0.755000000000 0.363500000000

0.520350000000 0.755000000000 0.363500000000

0.020350000000 0.245000000000 0.863500000000

0.520350000000 0.245000000000 0.863500000000

0.479650000000 0.245000000000 0.636500000000

0.979650000000 0.245000000000 0.636500000000

0.000000000000 0.101600000000 0.250000000000

0.500000000000 0.101600000000 0.250000000000

0.000000000000 0.898400000000 0.750000000000

0.500000000000 0.898400000000 0.750000000000

0.250000000000 0.601600000000 0.250000000000

0.750000000000 0.601600000000 0.250000000000

0.250000000000 0.398400000000 0.750000000000

0.750000000000 0.398400000000 0.750000000000

0.210750000000 0.604600000000 0.006400000000

0.710750000000 0.604600000000 0.006400000000

0.289250000000 0.604600000000 0.493600000000

0.789250000000 0.604600000000 0.493600000000

0.289250000000 0.395400000000 0.993600000000

0.789250000000 0.395400000000 0.993600000000

0.210750000000 0.395400000000 0.506400000000

0.710750000000 0.395400000000 0.506400000000

0.460750000000 0.104600000000 0.006400000000

0.960750000000 0.104600000000 0.006400000000

0.039250000000 0.104600000000 0.493600000000

0.539250000000 0.104600000000 0.493600000000

0.039250000000 0.895400000000 0.993600000000

0.539250000000 0.895400000000 0.993600000000

0.460750000000 0.895400000000 0.506400000000

0.960750000000 0.895400000000 0.506400000000

POSCAR file used for Montmorillonite.

System $Al_4Si_8O_{24}H_4$

1.00

5.18000000 0.00000000 0.00000000

0.00000000 8.97000000 0.00000000

-1.66202900 0.00000000 9.93189600

Al Si O H

4 8 24 4

Direct

0.000000000000 0.000000000000 0.000000000000

0.500000000000 0.500000000000 0.000000000000

0.000000000000 0.654000000000 0.000000000000

0.500000000000 0.154000000000 0.000000000000

0.432000000000 0.333000000000 0.270000000000

0.568000000000 0.333000000000 0.730000000000

0.932000000000 0.833000000000 0.270000000000

0.068000000000 0.833000000000 0.730000000000

0.432000000000 0.662000000000 0.270000000000

0.568000000000 0.662000000000 0.730000000000

0.932000000000 0.162000000000 0.270000000000

0.068000000000 0.162000000000 0.730000000000

0.489000000000 0.496000000000 0.335000000000

0.511000000000 0.496000000000 0.665000000000

0.989000000000 0.996000000000 0.335000000000

0.011000000000 0.996000000000 0.665000000000

0.173000000000 0.725000000000 0.335000000000

0.827000000000 0.725000000000 0.665000000000

0.673000000000 0.225000000000 0.335000000000

0.327000000000 0.225000000000 0.665000000000

0.170000000000 0.268000000000 0.320000000000

0.830000000000 0.268000000000 0.680000000000

0.670000000000 0.768000000000 0.320000000000

0.330000000000 0.768000000000 0.680000000000

0.334000000000 0.976000000000 0.105000000000

0.666000000000 0.976000000000 0.895000000000

0.834000000000 0.476000000000 0.105000000000

0.166000000000 0.476000000000 0.895000000000

0.417000000000 0.656000000000 0.109000000000

0.583000000000 0.656000000000 0.891000000000

0.917000000000 0.156000000000 0.109000000000

0.083000000000 0.156000000000 0.891000000000

0.343000000000 0.347000000000 0.109000000000

0.657000000000 0.347000000000 0.891000000000

0.843000000000 0.847000000000 0.109000000000

0.157000000000 0.847000000000 0.891000000000

0.934000000000 0.376000000000 0.105000000000

0.066000000000 0.376000000000 0.895000000000

0.434000000000 0.876000000000 0.105000000000

0.566000000000 0.876000000000 0.895000000000

APPENDIX B

Input files INCAR, and KPOINTS used for VASP calculation are listed for solvated Montmorillonite.

. **INCAR** file .

System = $N_{199}C_{727}O_{235}H_{1135}S_7$

ISMEAR = 0 ! Use 0 for KPOINTS less than 4 otherwise -5.

PREC = normal ! low, medium, normal are other options. Use suitable one.

ENCUT = 500 eV ! Decide considering the crystal size and accuracy you want.

EDIFF = 1.0E-4 ! Enegy difference covergence limit for electronic optimization.

EDIFFG = -1.0E-2 ! Enegy difference covergence limit for ionic optimization.

IBRION = 2 ! 0 for MD, 1 best, 2 for diff relaxation problems. Othere numbers for diffrent cases.

NSW = 250 ! Total number of ionic steps.

ISIF = 3 ! 2 and 4 ionic, 7 volume and 3 both.

LREAL = Auto ! Projection on real space. use FALSE (default) for reciprocal space.

NPAR = 64 ! Best sqrt of NCPUs used. should be ¿= NCPUs/32. ALGO = Fast ! default is Normal.

LCHARG = F ! No writting in CHG and CHGCAR files

LWAVE = F ! No writting in WAVECAR file

KPOINT file.

G

0

G

1 1 1

0 0 0

REFERENCE LIST

[1] Adhikari, P., Jawad, B., Rao, P., Podgornik, R., and Ching, W.-Y. Delta Variant with P681R Critical Mutation Revealed By Ultra-Large Atomic-Scale Ab Initio Simulation: Implications For The Fundamentals Of Biomolecular Interactions. *Viruses 14*, 3 (2022), 465.

[2] Al-saeedi, A. A. Clay Basics and Their Physical and Chemical Properties. *Iaetsd Journal for Advanced Research In Applied Sciences 10* (2022).

[3] Baral, K., Adhikari, P., Jawad, B., Podgornik, R., and Ching, W.-Y. Solvent effect on the structure and properties of RGD peptide (1FUV) at body temperature (310 K) using ab initio molecular dynamics. *Polymers 13*, 19 (2021), 3434.

[4] Baral, K., San, S., Sakidja, R., Couet, A., Sridharan, K., and Ching, W.-Y. Temperature-dependent properties of molten Li2BeF4 Salt using Ab initio molecular dynamics. *ACS omega 6*, 30 (2021), 19822–19835.

[5] Becke, A. D. Density-functional exchange-energy approximation with correct asymptotic behavior. *Physical review A 38*, 6 (1988), 3098.

[6] Blöchl, P. E. Projector augmented-wave method. *Physical review B 50*, 24 (1994), 17953.

[7] Brindley, G. W. *Clays, Clay Mineralsclays, Clay Minerals*. Springer US, Boston, MA,USA, 1983, pp. 69–80.

[8] Bylander, D., Kleinman, L., and Lee, S. Self-consistent calculations of the energy bands and bonding properties of B 12 C 3. *Physical Review B 42*, 2 (1990), 1394.

[9] Caruba, R., Baumer, A., Ganteaume, M., and Iacconi, P. An Experimental Study of Hydroxyl Groups and Water in Synthetic and Natural Zircons: A Model of The Metamict State. *American Mineralogist 70*, 11-12 (1985), 1224–1231.

[10] Ching, W. Theoretical Studies of The Electronic Properties of Ceramic Materials. *Journal of the American Ceramic Society 73*, 11 (1990), 3135–3160.

[11] Ching, W.-Y., and Rulis, P. *Electronic Structure Methods for Complex Materials: The Orthogonalized Linear Combination of Atomic Orbitals*. Oxford University Press, Oxford, UK, 2012.

[12] Ching, W.-Y., San, S., Zhou, C., and Sakidja, R. Ab Initio Simulation of Structure and Properties in Ni-Based Superalloys: Haynes282 and Inconel740. *Materials 16*, 2 (2023), 887.

[13] Davidson, A., and Vickers, A. The Optical Properties of Mica in the Vacuum Ultraviolet. *Journal of Physics C: Solid State Physics 5*, 8 (1972), 879.

[14] Davidson, E. Methods in computational molecular physics. In *NATO Advanced Study Institute, Series C* (1983), vol. 113, Plenum New York, p. 95.

[15] Detellier, C. Functional Kaolinite. *The Chemical Record 18*, 7-8 (2018), 868–877.

[16] Dharmawardhana, C., Misra, A., and Ching, W.-Y. Quantum Mechanical Metric for Internal Cohesion in Cement Crystals. *Scientific Reports 4*, 1 (2014), 1–8.

[17] Douillard, J.-M., Lantenois, S., Prelot, B., Zajac, J., and Henry, M. Study of The Influence of Location of Substitutions on The Surface Energy of Dioctahedral Smectites. *Journal of Colloid and Interface Science 325*, 1 (2008), 275–281.

[18] Essington, M. E. *Soil and Water Chemistry: An Integrative Approach.* CRC press, Boca Raton, FL, USA, 2015.

[19] Fang, Z.-J., Gou, K.-Y., Mo, M., Zeng, J.-S., He, H., Zhou, X., and Li, H. First-Principle Study of Electronic Structure of Montmorillonite at High Pressure. *Modern Physics Letters B 34*, 25 (2020), 2050263.

[20] Feig, M., Nawrocki, G., Yu, I., Wang, P.-h., and Sugita, Y. Challenges and Opportunities in Connecting Simulations with Experiments via Molecular Dynamics of Cellular Environments. *Journal of Physics: Conference Series 1036*, 1 (2018), 012010.

[21] Fernandes, M. M., and Baeyens, B. Cation Exchange and Surface Complexation of Lead on Montmorillonite and Illite Including Competitive Adsorption Effects. *Applied Geochemistry 100* (2019), 190–202.

[22] Gaillac, R., Pullumbi, P., and Coudert, F.-X. ELATE: An Open-Source Online Application for Analysis and Visualization of Elastic Tensors. *Journal of Physics: Condensed Matter 28*, 27 (2016), 275201.

[23] Gehr, P., and Heyder, J. *Particle-Lung Interactions.* CRC Press, 2000.

[24] Gianni, E., Avgoustakis, K., and Papoulis, D. Kaolinite Group Minerals: Applications in Cancer Diagnosis and Treatment. *European Journal of Pharmaceutics and Biopharmaceutics 154* (2020), 359–376.

[25] Giovannini, G., Garoli, D., Rupper, P., Neels, A., Rossi, R. M., and Boesel, L. F. Metal-Modified Montmorillonite as Plasmonic Microstructure for Direct Protein Detection. *Sensors 21*, 8 (2021), 2655.

[26] Hafner, J., and Kresse, G. The vienna ab-initio simulation program VASP: An efficient and versatile tool for studying the structural, dynamic, and electronic properties of materials. In *Properties of Complex Inorganic Solids*. Springer, 1997, pp. 69–82.

[27] Hartwell, J. The Diverse Uses of Montmorillonite. *Clay Minerals 6*, 2 (1965), 111–118.

[28] Hess, A. C., and Saunders, V. R. Periodic ab initio Hartree-Fock Calculations of The Low-Symmetry Mineral Kaolinite. *The Journal of Physical Chemistry 96*, 11 (1992), 4367–4374.

[29] Hill, R. The Elastic Behaviour of A Crystalline Aggregate. *Proceedings of the Physical Society. Section A 65*, 5 (1952), 349.

[30] Hohenberg, P., and Kohn, W. Inhomogeneous electron gas. *Physical review 136*, 3B (1964), B864.

[31] Honorio, T., Brochard, L., and Vandamme, M. Hydration Phase Diagram of Clay Particles from Molecular Simulations. *Langmuir 33*, 44 (2017), 12766–12776.

[32] Huggett, J. *Glauconites. Pp. 542À548 in: Encyclopedia of Geology (RC Selley, LRM Cocks, and IR Plimer, Editors).* Elsevier, Oxford, UK, 2005.

[33] Jawad, B., Poudel, L., Podgornik, R., Steinmetz, N. F., and Ching, W.-Y. Molecular mechanism and binding free energy of doxorubicin intercalation in DNA. *Physical Chemistry Chemical Physics 21*, 7 (2019), 3877–3893.

[34] Johnson, D. D. Modified Broyden's method for accelerating convergence in self-consistent calculations. *Physical Review B 38*, 18 (1988), 12807.

[35] Katti, D. R., Ghosh, P., Schmidt, S., and Katti, K. S. Mechanical Properties of The Sodium Montmorillonite Interlayer Intercalated with Amino Acids. *Biomacromolecules 6*, 6 (2005), 3276–3282.

[36] Keith, K., and Murray, H. *Clay Liners and Barriers*. Industrial minerals and rocks. Society for Mining, Metallurgy and Exploration, Littleton. Society for Mining, Metallurgy and Exploration, Littleton, 1994.

[37] Khaoulaf, R., Adhikari, P., Harcharras, M., Brouzi, K., Ez-Zahraouy, H., and Ching, W.-Y. Atomic-Scale Understanding of Structure and Properties of Complex Pyrophosphate Crystals by First-Principles Calculations. *Applied Sciences 9*, 5 (2019), 840.

[38] Kresse, G., and Furthmüller, J. Efficient Iterative Schemes for Ab Initio Total-Energy Calculations using A Plane-Wave Basis Set. *Physical Review B 54*, 16 (1996), 11169.

[39] Kresse, G., and Furthmüller, J. *Vienna Ab-initio Simulation Package (vasp)*. Austria, 2001.

[40] Kresse, G., and Hafner, J. Norm-conserving and ultrasoft pseudopotentials for first-row and transition elements. *Journal of Physics: Condensed Matter 6*, 40 (1994), 8245.

[41] Kresse, G., Hafner, J., and Needs, R. Optimized norm-conserving pseudopotentials. *Journal of Physics: Condensed Matter 4*, 36 (1992), 7451.

[42] Kresse, G., and Joubert, D. From Ultrasoft Pseudopotentials to The Projector Augmented-Wave Method. *Physical Review B 59*, 3 (1999), 1758.

[43] Lee, C., Yang, W., and Parr, R. G. Development of the Colle-Salvetti correlation-energy formula into a functional of the electron density. *Physical review B 37*, 2 (1988), 785.

[44] Li, N., and Ching, W.-Y. Structural, electronic and optical properties of a large random network model of amorphous SiO2 glass. *Journal of non-crystalline solids 383* (2014), 28–32.

[45] Liang, J.-J., and Hawthorne, F. C. Rietveld Refinement of Micaceous Materials; Muscovite-2M 1, A Comparison with Single-Crystal Structure Refinement. *The Canadian Mineralogist 34*, 1 (1996), 115–122.

[46] Liang, L., Rulis, P., Ouyang, L., and Ching, W.-Y. Ab initio investigation of hydrogen bonding and network structure in a supercooled model of water. *Physical Review B 83*, 2 (2011), 024201.

[47] Lorenz, P., Meier, L., and Kahr, G. Determination of The Cation Exchange Capacity (CEC) of Clay Minerals Using the Complexes of Copper (II) Ion with Triethylenetetramine and Tetraethylenepentamine. *Clays and Clay Minerals 47*, 3 (1999), 386–388.

[48] Luckham, P. F., and Rossi, S. The Colloidal and Rheological Properties of Bentonite Suspensions. *Advances in Colloid and Interface Science 82*, 1-3 (1999), 43–92.

[49] Man-Chao, H., Zhi-Jie, F., and Ping, Z. Atomic and Electronic Structures of Montmorillonite in Soft Rock. *Chinese Physics B 18*, 7 (2009), 2933.

[50] Marchuk, S., Rengasamy, P., and Churchman, J. Cation Exchange as Influenced by The Type of Cations in Different Clay Minerals. In *Proc., Australian Regolith and Clays Conf., Mildura, Australia*.

[51] Mavko, G., Mukerji, T., and Dvorkin, J. *The Rock Physics Handbook*. Cambridge university press, Cambridge, UK, 2020.

[52] Mhamdi, M., Gasmi, N., Elaloui, E., Kbir-Ariguib, N., and Trabelsi-Ayadi, M. Study of the Mechanical Properties of Clay Containing Smectite and Carbonate. *IOP Conference Series: Materials Science and Engineering 13*, 1 (2010), 012027.

[53] Miranda-Trevino, J. C., and Coles, C. A. Kaolinite Properties, Structure and Influence of Metal Retention on Ph. *Applied Clay Science 23*, 1-4 (2003), 133–139.

[54] Momma, K., and Izumi, F. VESTA 3 for Three-Dimensional Visualization of Crystal, Volumetric and Morphology Data. *Journal of Applied Crystallography 44*, 6 (2011), 1272–1276.

[55] Mondol, N., Jahren, J., Bjørlykke, K., and Brevik, I. Elastic Properties of Clay Minerals. *Geophysics 27* (2008), 758–770.

[56] Mulliken, R. Electronic population analysis on LCAO-MO molecular wave functions. IV. Bonding and antibonding in LCAO and valence-bond theories. *The Journal of Chemical Physics 23*, 12 (1955), 2343–2346.

[57] Mulliken, R. Overlap Populations, Bond Orders and Covalent Bond Energies. *J. Chem. Phys 23* (1955), 1841–1846.

[58] Mulliken, R. S. Electronic Population Analysis on LCAO–MO Molecular Wave Functions. I. *The Journal of Chemical Physics 23*, 10 (1955), 1833–1840.

[59] Murray, H. H. Overview—clay mineral applications. *Applied Clay Science 5*, 5-6 (1991), 379–395.

[60] Murray, H. H. Traditional and New Applications for Kaolin, Smectite, and Palygorskite: A General Overview. *Applied clay science 17*, 5-6 (2000), 207–221.

[61] Nielsen, O., and Martin, R. M. First-Principles Calculation of Stress. *Physical Review Letters 50*, 9 (1983), 697.

[62] Parr, R. G. *Density Functional Theory of Atoms and Molecules*. Springer, Berlin/Heidelberg, 1980, pp. 5–15.

[63] Patterson, J. D. Density-functional theory of atoms and molecules: Robert G. Parr and Weitao Yang. Oxford University Press, New York, and Clarendon Press, Oxford (1989). US 55.333*pages*, 1989.

[64] Perdew, J. P., Burke, K., and Ernzerhof, M. Generalized gradient approximation made simple. *Physical review letters 77*, 18 (1996), 3865.

[65] Perdew, J. P., Burke, K., and Ernzerhof, M. Generalized Gradient Approximation Made Simple. *Physical Review Letters 77*, 18 (1996), 3865.

[66] Poudel, L., Steinmetz, N. F., French, R. H., Parsegian, V. A., Podgornik, R., and Ching, W.-Y. Implication of the solvent effect, metal ions and topology in the electronic structure and hydrogen bonding of human telomeric G-quadruplex DNA. *Physical Chemistry Chemical Physics 18*, 31 (2016), 21573–21585.

[67] Pulay, P. Convergence acceleration of iterative sequences. The case of SCF iteration. *Chemical Physics Letters 73*, 2 (1980), 393–398.

[68] Pusch, R. Mechanical Properties of Clays and Clay Minerals. *Developments in Clay Science 1* (2006), 247–260.

[69] Radoslovich, E. The Structure of Muscovite, KAl2 (Si3Al) O10 (OH) 2. *Acta Crystallographica 13*, 11 (1960), 919–932.

[70] Reuß, A. Berechnung Der Fließgrenze Von Mischkristallen Auf Grund Der Plastizitätsbedingung Für Einkristalle. *ZAMM-Journal of Applied Mathematics and Mechanics/Zeitschrift für Angewandte Mathematik und Mechanik 9*, 1 (1929), 49–58.

[71] Richard, D., and Rendtorff, N. M. First Principles Study of Structural Properties and Electric Field Gradients in Kaolinite. *Applied Clay Science 169* (2019), 67–73.

[72] Sarkar, B., Rusmin, R., Ugochukwu, U. C., Mukhopadhyay, R., and Manjaiah, K. M. *Modified Clay Minerals for Environmental Applications*. Elsevier, Amsterdam, The Netherlands, 2019, pp. 113–127.

[73] Shafei, L., Adhikari, P., and Ching, W.-Y. DFT Study of Electronic Structure and Optical Properties of Kaolinite, Muscovite, and Montmorillonite. *Crystals 11*, 6 (2021), 618.

[74] Sparks, D. L. Kinetics of Ionic Reactions in Clay Minerals and Soils. *Advances in Agronomy 38* (1986), 231–266.

[75] Stadler, R., Wolf, W., Podloucky, R., Kresse, G., Furthmüller, J., and Hafner, J. Ab initio calculations of the cohesive, elastic, and dynamical properties of CoSi 2 by pseudopotential and all-electron techniques. *Physical Review B 54*, 3 (1996), 1729.

[76] Subramanian, N., Whittaker, M. L., Ophus, C., and Lammers, L. N. Structural Implications of Interfacial Hydrogen Bonding in Hydrated Wyoming-Montmorillonite Clay. *The Journal of Physical Chemistry C 124*, 16 (2020), 8697–8705.

[77] Sun, G., Kürti, J., Rajczy, P., Kertesz, M., Hafner, J., and , G. Performance of the Vienna Ab Initio Simulation Package (VASP) In Chemical Applications. *Journal of Molecular Structure: THEOCHEM 624*, 1-3 (2003), 37–45.

[78] Takata, M., Tomozawa, M., and Watson, E. Effect of Water Content on Transport in Na2O· 3SiO2 Glass. *Journal of the American Ceramic Society 65*, 2 (1982), 91–93.

[79] Tan, B. T., Wu, S., Anariba, F., and Wu, P. A DFT Study on Brittle-to-Ductile Transition of D022-Tial3 Using Multi-Doping and Strain-Engineered Effects. *Journal of Materials Science Technology 51* (2020), 180–192.

[80] Teich-McGoldrick, S. L., Greathouse, J. A., Jove-Colon, C. F., and Cygan, R. T. Swelling Properties of Montmorillonite and Beidellite Clay Minerals from Molecular Simulation: Comparison of Temperature, Interlayer Cation, and Charge Location Effects. *The Journal of Physical Chemistry C 119*, 36 (2015), 20880–20891.

[81] Tian, Y., Xu, B., and Zhao, Z. Microscopic Theory of Hardness and Design of Novel Superhard Crystals. *International Journal of Refractory Metals and Hard Materials 33* (2012), 93–106.

[82] Toth, R., Voorn, D.-J., Handgraaf, J.-W., Fraaije, J. G., Fermeglia, M., Pricl, S., and Posocco, P. Multiscale Computer Simulation Studies of Water-Based

Montmorillonite/Poly (Ethylene Oxide) Nanocomposites. *Macromolecules 42*, 21 (2009), 8260–8270.

[83] Vanderbilt, D. Soft self-consistent pseudopotentials in a generalized eigenvalue formalism. *Physical review B 41*, 11 (1990), 7892.

[84] Vanorio, T., Prasad, M., and Nur, A. Elastic Properties of Dry Clay Mineral Aggregates, Suspensions and Sandstones. *Geophysical Journal International 155*, 1 (2003), 319–326.

[85] Voigt, W. *Lehrbuch der kristallphysik:(mit ausschluss der kristalloptik)*, vol. 34. BG Teubner, 1910.

[86] Walker, B., Dharmawardhana, C. C., Dari, N., Rulis, P., and Ching, W.-Y. Electronic structure and optical properties of amorphous GeO2 in comparison to amorphous SiO2. *Journal of Non-Crystalline Solids 428* (2015), 176–183.

[87] Wang, J., Kalinichev, A. G., Kirkpatrick, R. J., and Cygan, R. T. Structure, Energetics, and Dynamics of Water Adsorbed on The Muscovite (001) Surface: A Molecular Dynamics Simulation. *The Journal of Physical Chemistry B 109*, 33 (2005), 15893–15905.

[88] Wang, Z., Wang, H., and Cates, M. E. Effective Elastic Properties of Solid Clays. *Geophysics 66*, 2 (2001), 428–440.

[89] Wood, D., and Zunger, A. A new method for diagonalising large matrices. *Journal of Physics A: Mathematical and General 18*, 9 (1985), 1343.

[90] Xiong, M., Zhao, X., Yin, G., Ching, W.-Y., and Li, N. Unraveling the effects of linker substitution on structural, electronic and optical properties of amorphous zeolitic imidazolate frameworks-62 (a-ZIF-62) glasses: a DFT study. *RSC advances 10*, 24 (2020), 14013–14024.

[91] Yao, H., Ouyang, L., and Ching, W. Ab initio Calculation of Elastic Constants of Ceramic Crystals. *Journal of the American Ceramic Society 90*, 10 (2007), 3194–3204.

[92] Yavuz, , Altunkaynak, Y., and Güzel, F. Removal of Copper, Nickel, Cobalt and Manganese from Aqueous Solution by Kaolinite. *Water Research 37*, 4 (2003), 948–952.

[93] Young, D. *Computational Chemistry: A Practical Guide for Applying Techniques to Real World Problems*. John Wiley Sons, Hoboken, NJ, USA, 2004.

[94] Yu, C.-J., Choe, S.-H., Jang, Y.-M., Jang, G.-H., and Pae, Y.-H. First-Principles Study of Organically Modified Muscovite Mica with Ammonium Or Methylammonium Ion. *Journal of Materials Science 51*, 24 (2016), 10806–10818.

[95] Zhang, Y., Luo, Y., Guo, X., Xia, T., Wang, T., Jia, H., and Zhu, L. Charge Mediated Interaction of Polystyrene Nanoplastic (PSNP) with Minerals in Aqueous Phase. *Water Research 178* (2020), 115861.

[96] Škundrić, T., Matović, B., Zarubica, A., Zagorac, J., Tatarko, P., and Zagorac, D. Structure Prediction and Mechanical Properties of Silicon Hexaboride on Ab Initio Level. *Materials 14*, 24 (2021), 7887.

VITA

Layla Shafei was born on June 28, 1998, in Jeddah City, Kingdom of Saudi Arabia, and began her academic journey by earning a B.S. in Physics from King Abdul-Aziz University in 2012. Her profound passion for physics ignited a thirst for knowledge and propelled her toward higher academic achievements. This fervor led her to the United States, where she successfully completed her master's degree in Physics at the University of Missouri-Kansas City in 2016. Then She got the opportunity at Al-Jouf University to work as a lecturer of physics.

Subsequently, Layla embarked on a Ph.D. program, specializing in Physics with a complementary focus on Mathematics. During her doctoral studies, she was an active member of the Electronic Structure Group at UMKC, working under the guidance of the esteemed Curators' Distinguished Professor of Physics, Dr. Wai-Yim Ching.

Layla's dedication to her field resulted in the publication of two research papers as the primary author and one as a co-author in respected peer-reviewed journals. Furthermore, she showcased her research contributions by delivering two conference talks, presenting one conference poster, and participating in a university symposium poster presentation.

PUBLICATIONS

1. **Shafei, L**., Adhikari, P., San, S., Ching, W. Y. (2023). Electronic Structure and Mechanical Properties of Solvated Montmorillonite Clay Using Large-Scale DFT Method. Crystals, 13(7), 1120.

2. **Shafei, L**., Adhikari, P., Ching, W. Y. (2021). DFT study of electronic structure and optical properties of kaolinite, muscovite, and montmorillonite. Crystals, 11(6), 618.

3. Adhikari, P., **Shafei, L.**, San, S., Rulis, P., Ching, W. Y. (2020). Origin of the existence of inter-granular glassy films in -Si3N4. Journal of the American Ceramic Society, 103(2), 737-743.